SYNTHESIS ROUTE FOR CESIUM AND THIOCYANATE DOPED HALIDE PEROVSKITE THIN FILMS FOR A NEW GENERATION OF SOLAR CELLS

A thesis submitted for the degree of master

Mónica María López Paz

Chemical Engineer

Advisor

Dr. Miguel Ángel Uribe Laverde

Co-advisor

Dr. Angela Patricia Pardo González

Universidad de La Sabana

UNIVERSIDAD DE LA SABANA

FACULTY OF ENGINEERING

MASTER IN PROCESS DESIGN AND MANAGEMENT, CHEMICAL PROCESSES MAJOR, RESEARCH MODE

CHÍA, CUNDINAMARCA

2021

Acknowledgments

I would like to thank my academic supervisors Miguel and Angela, for providing guidance, support, and feedback, also for their patience, good attitude, time, and interest during this journey. Thanks also to my partner for his encouragement and company. Thanks to my parents for their moral support. I would like to thank Sergio my colleague for his passionate work, patience, and compromise in this research.

Also, thanks to Camilo and Ricardo for their invaluable help at Fablab laboratories. Thanks to all the people who contributed to this research Juan Camilo, Cristian, Daniela, Lina, Diego, Benny, Maria Alejandra, university professors who advised me and collaborated with this project, colleagues, and lab technicians. I could not have done any of this without your help.

"Everybody knows, but you have got to stop and think about it, to really get the pleasure about the complexity, the inconceivable nature of Nature."

Richard Feynman

Table of contents

Table of figures

Table index

List of symbols and abbreviations

BSD: Back scattered detector

ETL: Electron transporting layer

FTO: Fluor tin oxide

HTL: Hole transporting layer

ITO: Indium tin oxide

PCE: Power conversion efficiency

PVK: Perovskite

SEM: Scanning electron microscopy

XRD: X-ray diffraction

Abstract

A novel, efficient, low-cost, and long-term lifetime photovoltaic technology is essential for accelerating the energy transition to renewable energy sources. Perovskite thin films stand out as promising photovoltaic technologies due to competitive power conversion efficiencies over 20% and low-cost fabrication techniques [1]. Nevertheless, this technology is still affected by short lifetimes that are consequence of the strong sensitivity of the pristine perovskites to effects such as moisture, UV radiation, and the presence of oxygen. Doping the perovskite materials to change their intrinsic properties and increase their stability is one of the proposed solutions to this issue [2]. In this work, we study the synthesis route to fabricate the double partial substitution with cesium and thiocyanate (SCN) in the methylammonium (MA) and iodide sites, respectively, of the pristine perovskite compound $MAPbI_3$. Individually, these substitutions have shown to enhance the structural stability of the perovskites and increase their resistance to moisture and ambient conditions. However, to the best of our knowledge, the proposed double substitution has not been studied. The project's first stage was manufacturing an acrylic glove box. This process included the design, cut of acrylic sheets, sanding, assembling, and tuning of the system. The second stage was preparing perovskite precursor solutions according to predefined stoichiometry amounts of thiocyanate, methylammonium, and cesium. In the third stage, perovskite thin films were deposited on a glass substrate, annealed on a hot plate, and characterized by means of scanning electron microscopy (SEM) x-ray diffraction (XRD) and IR-VIS absorption spectroscopy. The synthesis process uses the one-step spin-coating technique, chlorobenzene as an antisolvent, and a substrate preheating stage. Following the established synthesis process we have synthesized high quality thin films with the pristine perovskite composition. According to XRD, only a small presence of lead iodide can be identified as an impurity. The bandgap calculated from absorption measurements is 1.56 eV. Upon the inclusion of cesium, the

bandgap increases to 1.60 eV, confirming the effective incorporation of cesium ions into the perovskite structure. This effective substitution is further confirmed by the changes lattice parameters as determined by XRD measurements. However, we notice that the substitution is effective only up to a 7% cesium doping. Above this value, significant impurities can be identified and no further changes in the bandgap are observed. Using a 7% cesium doping, we proceed to synthesize thin films with thiocyanate substitution levels of 7% and 14%. In this case, however, the thiocyanate does not incorporate into the perovskite structure as suggested by the observation of no significant changes in the bandgap. Moreover, in this case we observed that the samples experienced a fast decay into a yellowish transparent phase that, according to XRD, is composed of the precursor components in a largely amorphous configuration. Therefore, the proposed one-step synthesis procedure is not suitable to achieve the double substitution of cesium and thiocyanate in the perovskite structure. Further research using other deposition methods such as two-step spin coating or dip coating must be carried out to obtain the desired substitution.

Keywords: Perovskite, doping, thiocyanate, cesium, characterization, light harvesters, one-step, antisolvent, chlorobenzene.

Resumen

Una tecnología fotovoltaica novedosa, eficiente, económica y con un tiempo de vida prolongado es crucial para acelerar la transición energética a fuentes de energía renovables. Las películas delgadas de perovskita son promisorias ya que las celdas solares de este material poseen eficiencias competitivas que sobrepasan el 20% y métodos de fabricación a bajo costo [1]. Sin embargo, esta tecnología tiene una desventaja, se degradan rápidamente como consecuencia de la humedad, radiación UV y presencia de oxígeno. El dopaje de los compuestos de perovskita es una de los soluciones planteadas a los problemas de estabilidad, puesto que se pueden cambiar sus propiedades intrínsecas, mejorando su estabilidad [2]. Este trabajo estudia la ruta de fabricaion de perovskitas doblemente dopadas con cesio (Cs) y tiocianaton (SCN), en los sitios del yoduro de metilo (MAI) y del yodo, respectivamente, de un compuesto de perovskita pristina $MAPbI_3$. Individualmente, estas sustituciones han demostrado una mejora en la estabilidad, aumentando su resistencia a la humedad y a las condiciones ambientales.

La primera etapa del proyecto consistió en la fabricación de una caja de guantes de acrílico. Se desarrolló el diseño, el corte , el ensamble y la puesta a punto de la caja. En la segunda etapa se fabricaron las películas delgadas según unas estequiometrias preestablecidas de tiocianato, MAI y cesio. La tercera etapa comprendió el depósito de las películas sobre sustratos de vidrio, un recocimiento en una plancha de calentamiento y su posterior caracterización a través de microscopia electrónica de barrido (SEM por sus siglas en ingles), difracción de rayos-x (XRD) y espectroscopia de absorción en el rango del infrarrojo-visible. El proceso de síntesis planteado sigue la metodología de recubrimiento por centrifugación de un paso y sugiere el uso de clorobenceno como antisolvente y un precalentamiento. Siguiendo los parámetros de síntesis establecidos, hemos sintetizado películas delgadas prístinas de alta calidad. Según los resultados de XRD, solo una pequeña cantidad de yoduro de plomo. El bandgap calculado a partir

de las medidas de absorbancia es de 1.56 eV. Al incluir cesio en la estructura, el bandgap determinado aumento a 1.60 eV, confirmando así su inserción en la estructura. Esto se reafirma por el cambio en los parámetros de red encontrados en las medidas de XRD. Es importante resaltar que la sustitución resultó efectiva hasta un 7% de dopaje de cesio. Al sobrepasar este porcentaje, hay una presencia significativa de impurezas y el bandgap no cambia. Posteriormente, se realizó la sustitución doble de cesio y tiocianato, manteniendo el dopaje de cesio en 7%. En este caso se evidencio en las medias de absorbancia que no hubo cambios en el bandgap indicando la no inserción de tiocianato. Las muestras doblemente dopadas se descompusieron rápidamente, tornándose amarillas y transparentes, en este caso los resultados de XRD indicaron la presencia de una fase amorfa. Ahora bien, el proceso de fabricación de un paso no es apropiado para hacer el doble dopaje. Posteriores investigaciones empleando recubrimientos por inmersión o por centrifugación en dos pasos puede realizarse para obtener la sustitución deseada.

Palabras clave: Perovskita, dopaje, tiocianato, cesio, caracterización, absorbedores de luz, metodología de un paso, antisolvente, clorobenceno.

Graphic Abstract
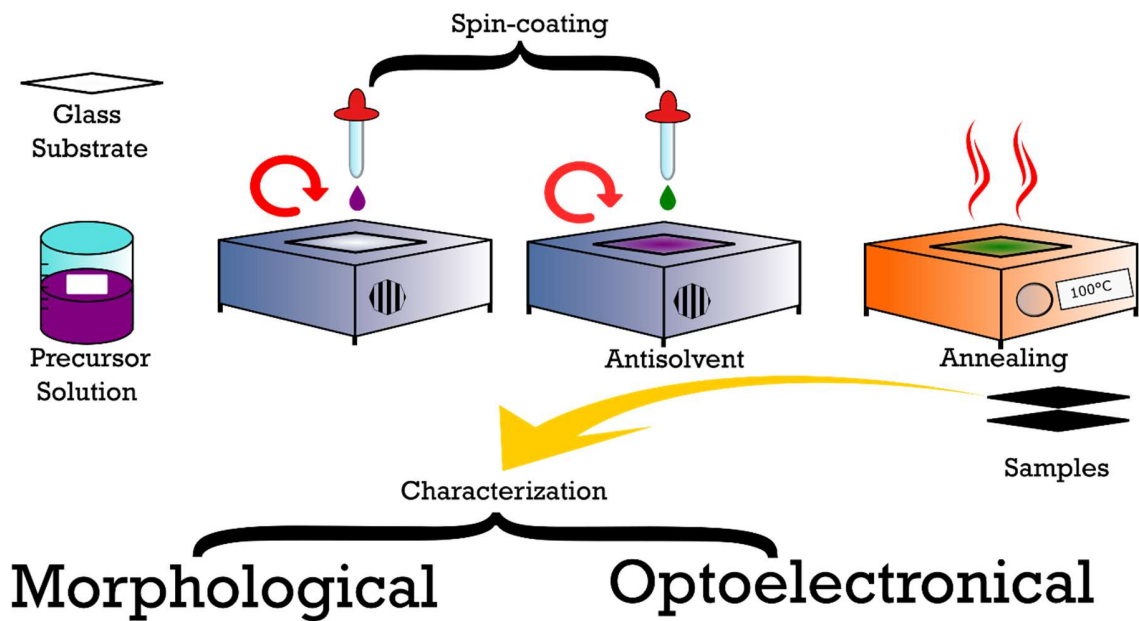
Figure 1. Graphical abstract.The one-step perovskite fabrication procedure at a glance. Thin films are deposited on top of glass substrate. Next, spin-coated before finishing the spin-coater sequence a drop of antisolvent is added. Finally, samples are annealed and characterized.

INTRODUCTION

1. GENERAL INTRODUCTION AND JUSTIFICATION

Energy production and supply is one of the biggest challenges faced by humankind. Increasing energy demands are predicted by the International Atomic Energy Agency (IAEA); according to this agency, the world energy consumption is projected to increase by 18% by 2030 and by 39% by 2050 [3]. Ascending incomes, increasing population, and the general development of the economies, as stated by the International Energy Agency (IEA), are the leading causes of rising global energy demands [4]. Furthermore, energy transition is being forced by factors such as climate change. The leading cause of climate change is the combustion of fossil fuels to fulfill global energy demands [5]. Therefore, replacing conventional carbon fossil energy sources is an urgent response to climate change. Consequently, cleaner energy production has been included in the top 10 sustainable development goals defined by the United Nations [6]. Pathways for a sustainable energy transition consider decarbonizing energy production employing renewable energy sources, primarily focusing on solar energy through photovoltaic technologies and wind energy [7].

Solar energy is a prominent abundant energy source. It stands out on the renewable energy sources because the sun reaches the Earth's surface as heat and light with around 18 000 TW, which strongly contrasts with the 12 TW of global energy demand [8]. We could explode that potential off using technologies like solar heaters or photovoltaic technologies through solar panels to obtain electricity. Solar panels consist of several connected solar cells. Solar cells are illuminated by sunlight and directly convert photons into electricity [9]. These devices consist of semiconductor materials to absorb light. Electrons are excited from the valence to the conduction band upon the absorption of sunlight photons. This movement gives rise to the

electron-hole pairs responsible for the charge separation effect that results in electricity. [8].

Photovoltaic technologies are grouped into four generations [9]. The first one consists of mature, fully commercial silicon wafer-based solar modules. The second one is thin-film-based, and it incorporates materials such as amorphous silicon, cadmium telluride, copper indium selenide, and copper indium gallium selenide as the active layer. The third generation is based on developing (novel and emerging materials) technologies and includes organic solar cells and other emerging materials [10]. Finally, the fourth generation of photovoltaic devices includes novel materials such as perovskite (PVK) solar cells that belong to thin-film technologies [11].

The main advantage of the novel PVK solar cells is their high absorption coefficients, which allow for thin photovoltaic devices with active layers about ~300 to 900 nm thickness. Typical crystalline silicon layers are around ~100 to 500 μm due to an indirect bandgap and lower absorption coefficients. Also, in thin-film CdTe-based devices, the thickness is in the order of ~4 to 6 μm [11], [12]. PVK materials are more efficient than first-generation silicon solar cells in a range of 1-100 times [9]. Thin-film technologies reduce solar cell manufacturing costs because the semiconductor layer requires less active material to harvest light from the sun than conventional wafer-based silicon modules, which results in lower fabrication costs and lower energy payback times [10]. The Energy Payback time is the time taken by photovoltaic systems to produce the same amount of energy used to fabricate and dispose them, from raw materials extraction to dismantlement. For example, mature technologies from first-generation solar modules of monocrystalline silicon solar cells have a payback time ranging from 1.4 to 7.3 years, depending on the location, whereas PVK based modules (representative technologies of fourth-generation) exhibit energy payback times between 0.2 and 5.4 years [13].

The golden triangle evaluates photovoltaic technologies with three factors: cost, efficiency, and lifetime [14]. **Figure 2** summarizes the golden triangle for the first-generation silicon modules and the fourth-generation PVK based modules. The comparison between PVK and silicon technologies evidence that production costs are less than half for PVK solar cells than for monocrystalline silicon solar cells [14]. The manufacturing process of silicon modules is highly energy-consuming due to the need to purify the silicon up to solar grade, known as 5N, which corresponds to a purity of 99. 999% [15].

On the other hand, the efficiency exhibits similar values of about 26.1% for silicon and 25.2% for PVK [16]. However, it is remarkable that the perovskite technologies appeared in 2009, and their efficiencies have passed from 3.9% to 25.2% in just over a decade [17], [18]. Finally, the lifetime is defined as T_{80}, the time it takes for a solar module to get its efficiency reduced to 80% of its initial performance [15]. In this regard, there is a significant difference between silicon and PVK solar cells. While the former exhibits a lifetime of around 25 years, the latter shows a lifetime of 1 year. This striking difference comes from PVK stability issues, which drastically shorten their lifetime under normal atmospheric conditions. These stability issues are the main delayers of large-scale manufacturing for PVK solar cells.

PVK as novel materials for photovoltaic applications are challenged by material degradation, making them unable to compete with traditional silicon solar cells and delaying PVK large-scale manufacturing and further commercialization. Before large-scale manufacturing, handling PVK stability issues is compulsory to complete the golden triangle of photovoltaic technologies and make PVK solar cells competitive in the solar market [19]. PVK stability issues are caused by moisture, ion migration, UV radiation, thermal and structural instability [20]. High quality, efficient with extended lifetime PVK thin films are determined by controlled morphology, thickness uniformity, minimum pinholes, material PVK phase purity, and high crystallinity [14]. Optimizing PVK active layer involves engineering PVK composition,

fabrication method, control of crystallization using antisolvents, substrate, and solvent selection [21].
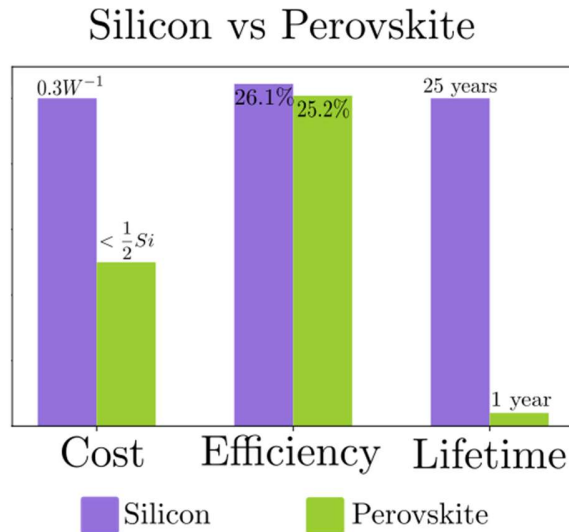
Figure 2. *The golden triangle of photovoltaic technologies for monocrystalline silicon and perovskites. Cost, efficiency, and lifetime are compared for both technologies. Adapted from [14] and [16], certified record efficiencies are up to date.*

Regarding PVK composition, several strategies have been implemented to enhance stability: ion substitutions through doping with cesium [22], [23], thiocyanate[24], [25], and rubidium [26] have been reported. Cesium doping on the PVK lattice leads to better stability when compared to pristine PVK methylammonium lead iodide (MAPbI$_3$) and better light absorption and morphology [22]. On the other hand, it has been reported that thiocyanate allows the fabrication of PVK under high relative humidity, overcoming the moisture instability [24]. Nevertheless, to the best of our knowledge there is no literature reporting a double substitution with cesium and thiocyanate for enhancing PVK stability. This is the main goal of this research project.

Climate change is a common concern for humankind. The Paris Agreement recognizes "the need for an effective and progressive response to the urgent threat of climate change based on the best available scientific knowledge…" [27]. Countries

under the Paris Agreement are implementing national projects and laws promoting low-carbon technologies for decarbonization in different sectors, such as energy production using renewable sources for energy transition [28]. Integrating wind and solar energy is a critical pathway for energy transition [29]. Big projects such as Photovoltaic Power Systems Programme (PVPS), with a total of 32 participant countries in all continents, stand out and pave the way for cleaner energy production [30].

According to Banco Interamericano de Desarrollo (Inter-American Development Bank), there are three major transformational projects related to the energy sector in Colombia: Programa de Eficiencia Energética del Caribe Colombiano (Colombian Caribbean Energy Efficiency Program), Programa de Acceso Universal (Universal Access Program), and Reforma Regulatoria del Mercado de Energía Mayorista, Integración Energética Regional y Digitalización (Regulatory Reform of the Wholesale Energy Market, Regional Energy Integration and Digitization) [31], implementing these projects the Colombian National Government seeks to modernize the institutional and regulatory framework of the electricity sector, facilitating the incorporation of new agents, technologies and transactional schemes in the energy market [32].

Now, the three projects are briefly described as follows: The Energy Efficiency Program in the Colombian Caribbean will promote the introduction of more efficient technologies and processes, the use of renewable Non-Conventional Energy Sources, and demand management in priority consumption sectors [31]. Furthermore, the Universal Access Program aligns with the seventh goal from Sustainable Development Goals, "Affordable and Clean Energy" [6]. In addition, the national government settled a deadline in 2022 to increase the coverage of the electric energy service, benefiting 100,000 new users, raising the installed electric power generation capacity from 16,420 MW to 19,159 MW.

Furthermore Non-Conventional Energy Sources also exhibit a growing generation capacity of 1,500 MW in 2020, up from 22.4 MW in 2018 [33], [34]. The Regulatory Reform of the Wholesale Energy Market Regional Energy Integration and Digitization program consists of stimulating structural reforms in the wholesale energy market and also strengthening the Andean Electrical Interconnection System SINEA (Chile, Bolivia, Colombia, Ecuador, and Peru) and promoting the incorporation of new information technologies [31].

On the other hand, Colombia also has policies regarding energy transition, such as the 2014 established law 1715 and guidelines for including non-conventional energy sources on the national energy matrix as stated by Misión de la Transición energética (Mission of Energy Transition) from Ministerio de Minas y Energía, (Ministry of Mines and Energy) [32] based on the Paris agreement. Law 1715 is the legal framework for integrating non-conventional energy sources, mainly those that manage renewable energy sources. Government entities such as Ministerio de Minas y Energía, Comisión de Regulación de Energía y Gas (Energy and Gas Regulatory Commission, CREG), Unidad de Planeación Minero Energética (Mining and Energy Planning Unit, UPME) and the Ministerio de Ambiente y Desarrollo Sostenible (Ministry of Environment and Sustainable Development) have been assigned functions within the regulatory framework [35]. The policies and projects regarding energy transition and efficiency of the Colombian national government are focused on the commitment to close some inequality gaps, as is the case of the coverage of public services and how electricity has the power to change lives, where territories without energy have a limiting factor for social, economic and sustainable development [36]

Energy transition to renewable sources requires large-scale manufactured photovoltaic devices to fulfill the big projects' energy demands. Novel materials, such as PVK solar cells will be in scalable manufacturing only after becoming competitive and surpassing stability issues for completing the photovoltaic golden triangle.

Following the vision of Ministerio de Ciencia y Tecnología (Ministry of Science and Technology) regarding Colombia's transformation into a knowledge-based society, this project aims to study the effects of the double substitution of cesium and thiocyanate on the optical and structural properties of PVK thin films grown on FTO coated glass substrates. The impact caused by mixing cations combines the advantages of every constituent and helps to dodge their downsides [37]. Making a double partial substitution to the pristine PVK with cesium and thiocyanate could enhance the intrinsic stability under non-controlled atmospheres. We expect that our findings pave the way for easy fabrication procedures under high relative humidity (50%-80%) and stable PVK thin films under atmospheric conditions. More straightforward manufacturing methods lead to lower production costs, and PVK thin film stability makes these materials competitive in the solar market, allowing affordable and clean energy. Since there are no studies regarding cesium and thiocyanate double substitutions, we are led to the following research question: What are the cesium and thiocyanate doping conditions in hybrid lead halide perovskites to maximize their suitability to develop thin-film solar cells through the spin coating deposition?

2. BACKGROUND

2.1. Perovskite

PVK emerged in 2009 as novel material to fabricate thin-film solar cells [38]. PVK compounds have ABX_3 as their general chemical formula. PVK crystal structures form a pseudo-cubic array of octahedra composed of BX_6 [39], as shown in **Figure 3**. Hybrid lead halide PVKs have cations on A and B sites. A is a large organic cation where, in principle, any molecular cation could be used if it fits into the octahedra cavity [40]. B could be lead or tin, and X is a halogen anion such as Cl, Br, or I. PVK chemistry depends on atoms occupying the A, B, and X sites [41], [42]. For instance, PVK optical properties can be tuned by ion substitution [43].
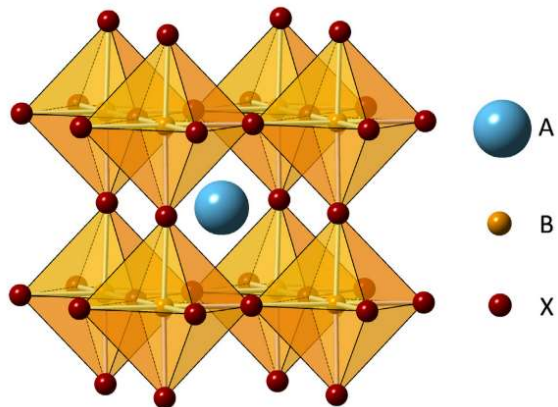
Figure 3. *Perovskite crystal structure. A site represents a cation, B site Pb or Sn and X site Cl, Br or I. Image retrieved from* [43]*.*

2.1.1. PVK properties

Optoelectronic properties in PVK material depend mainly on the ions occupying the B and X sites. These materials are suitable for photovoltaic applications because of their strong light absorption in the visible region. The solar radiation spectrum is shown in **Figure 4**, on top of the spectrum the PVK absorption range is shown. As can be seen, the PVK absorption range lies in the region where most of the solar spectrum energy is received [44], in the entire visible to near-infrared zones [45]. The absorption takes place in the PVK octahedral structure [41]. Also, PVKs have a direct bandgap and it is possible to tune their bandgap through chemical modification of the anion (site B). For example, pristine PVK comprises methylammonium, lead and iodine $MAPbI_3$, and the bandgap can be changed between 1.5 eV to 2.3 eV upon insertion of Br changing the composition to $MAPb(Br_xI_{1-x})_3$ [21].
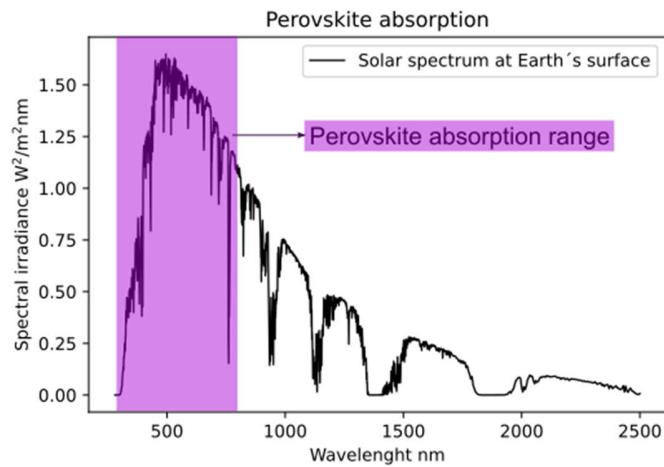
Figure 4. *Perovskite absorption spectrum. The black line represents the solar spectrum at Earth's surface. Absorption for the perovskite is shadowed in purple. Data retrieved from* [16].

2.2 Perovskite solar cells

Nowadays, high-performance PVK solar cells have as active layer PVK crystal structures which are placed between an electron transporting layer (ETL) and a hole transporting layer (HTL) [43]. All layers are usually manufactured by solution-processed methods and achieve power conversion efficiencies (PCEs) up to 25.2% [46]. The working principle of PVK solar cells is based on the interaction of five actors, as shown in **Figure 5** and explained in more detail as follows:

- **Layer a)** is the back electrode (metal) is, in general, evaporated gold or silver layer.
- **Layer b)** presents the HTL, a p-type semiconductor. It extracts holes from PVK active layer. Typically, 2,2′,7,7′-tetrakis(N,N-dip-methoxyphenylamine)-9,9′-pirobifluorene (spiro-OMeTAD) is used.
- **Layer c)** is the PVK layer, typically the methylammonium lead iodide $MAPbI_3$
- **Layer d)** presents the ETL. It is constructed based on an n-type semiconductor. It is characterized by high electron mobility and effectively extracting electrons from the PVK active layer. Typically, fullerene derivatives

and n-type metal oxides, usually a mesoporous or planar layer of titanium dioxide TiO_2 is implemented [47].

- **Layer e)** layer is the front transparent electrode: PVK solar cells typically contain fluorine-doped tin oxide (FTO) or Indium tin oxide (ITO) as transparent electrodes [43].
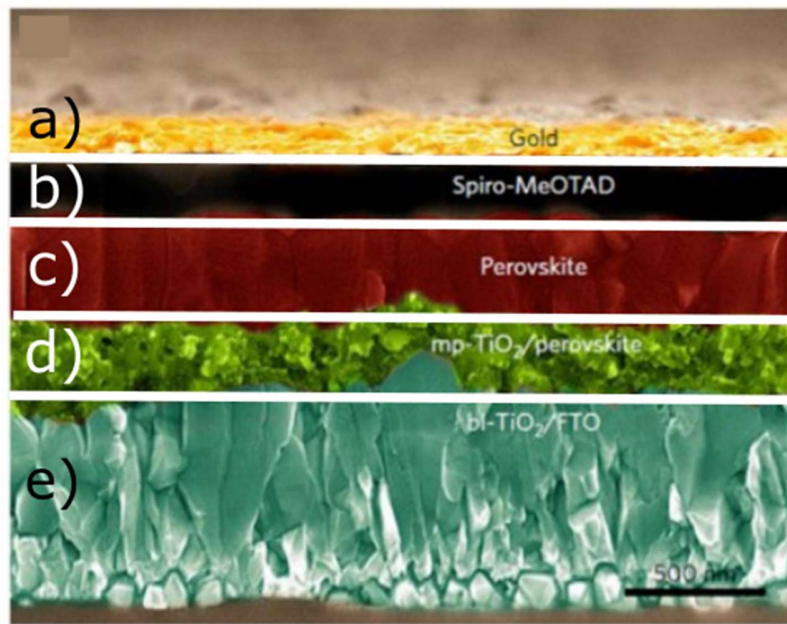
Figure 5. Perovskite solar cell architecture. Scanning electron microscopy (SEM) image for a perovskite solar cell with the typical architecture with gold as a metal electrode, spiro-OMeTAD as HTL, perovskite active layer, titanium dioxide as ETL, and FTO as a transparent electrode. Image retrieved and adapted from [21].

The interaction is based on the band to band transitions and has three processes: first, photon absorption in the PVK layer and generation of free charges, an electron in the conduction band, and a hole in the valence band. Second, the free charges move towards their energetically favorable layers driven by the built-in electric field. Electrons and holes separate and move to the ETL and the HTL, respectively. Finally, the charges are extracted at the conducting electrodes [43], [47].

2.3 Perovskite fabrication

PVK layers are fabricated through vacuum deposition, solution-processed methods, vapor-assisted solution deposition, vacuum-flash assisted deposition, and flash infrared annealing methods [48]. Thin-film defects are primarily originated from fabrication conditions. Deposition methods strongly influence grain sizes, electron and hole mobilities, and, as a consequence, device performance. [47] Nowadays, solution-processed methods and spin-coating are widely used at laboratory scales and are sorted as one and two-step [49]. Solution-processed methods consist of the deposition of the precursor solution on a substrate [45]. The one-step procedure involves spin-coating the precursor solution containing all the PVK constituents diluted in solvents and the subsequent annealing process. The two-step process, on the other hand, involves sequential reactions while depositing the lead precursors first, followed by the organic components, and finally an annealing process to transform to the PVK phase [48].

Another variation of the fabrication is the antisolvent method, which is shown in **Figure 6**. It is a treatment for morphological optimization and consists of adding a non-polar solvent, which has an affinity with the solvent employed on precursor solutions but is insoluble with PVK precursors [50]. Antisolvent has an essential role in spin coating methodology because although most of the solvent is removed by high-speed rotation, there are always remaining amounts of solvent still present. This solvent is later slowly released in the annealing step, impacting negatively the thin-film morphology. Antisolvent addition favors rapid crystallization leading to high-quality PVK thin films [51]. Antisolvent is added during spin-coating leading to fast nucleation and the subsequent thermal annealing resulting in high-quality PVK thin films [50].
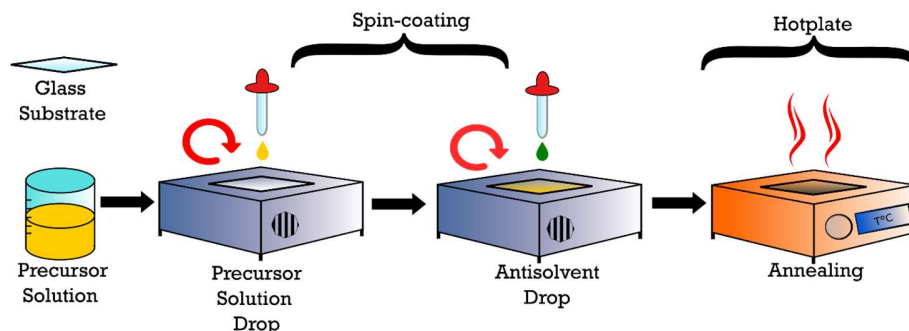
Figure 6. *Summary of the antisolvent method. It has four stages, precursor solution stirring, perovskite precursor drop, antisolvent drop, and thermal annealing.*

Antisolvent addition has advantages such as improving surface coverage, increased grain size, higher crystallinity, reduced film roughness leading to better photovoltaic performance, and PVK thin film stability. Common antisolvents employed are toluene, trifluorotoluene, chlorobenzene, diethyl ether, acetonitrile, dichloromethane, and petroleum ether. In addition, N-hexane, isooctane, phenetole, anisole, ethanol, ethyl acetate, methyl benzoate, methyl butyrate, and isopropanol represent alternative green antisolvents [51].

High-quality PVK thin films.

High-quality thin films are determined by controlled morphology (grain size and size uniformity), thickness uniformity, phase purity, and high crystallinity. Regarding controlled morphology, large grains are preferred. Furthermore, high crystallinity is a relevant factor for photovoltaics applications because it determines charge separation efficiency, charge transport, and diffusion length [21].

2.4 Stability

Cost, efficiency, and lifetime or stability are the three factors of the golden triangle of photovoltaic technologies. Economic assessments support the potential of PVK solar cells with costs around one-half of the conventional silicon solar cells [14]. In addition, PVK solar cells have a record efficiency of 25.2%, comparable to 26.1% for silicon [16]. Nevertheless, PVK solar cells struggle with stability issues, with a

maximum lifetime reported of around one year in contrast with 25 years of silicon lifetime [14]. Stability issues are divided into three stages: materials, single cells, and modules [19]. Regarding material instability, PVKs are sensitive to environmental conditions, especially moisture present in ambient air, material degradation, temperature, and UV radiation [49], [20].

- Moisture. The chemical process of hydrolyzation causes PVK decomposition due to water because of PVK polarity. Water reacts with the proton of the PVK layer resulting in PbI_2 [52].

- Thermal instability. PVK materials are sensitive to heat resulting in phase transitions. PVK crystal structure is orthorhombic at temperatures below -110 °C, it is tetragonal at temperatures between -110 °C and 54.25 °C, and cubic above 54.25 °C [52].

- UV radiation. Photogenerated electrons from the PVK layer form superoxide with molecular oxygen present in the air. Subsequently, it reacts with MA because it has acid protons [20].

2.5 Materials characterization

Characterization techniques are crucial for evaluating PVK thin films at three regimes: chemistry, fabrication, and performance. The first is related to the electronic band structure and the chemical composition. The second is focused on morphology and crystallography. And the last one depends on carrier dynamics [53]. For proposing a synthesis route, the chemistry and the fabrication regime are the most relevant characterizations. Absorption spectroscopy UV-Vis (UV-Vis), Scanning Electron Microscopy (SEM), and X-Ray Diffraction (XRD) are explained in more detail in the next section.

- **Chemistry regime**

Absorption spectroscopy UV-Vis: Electronic band structure information is evaluated through the spectra generated by this characterization technique. Spectroscopy

13

characterizations explore the interaction of waves with matter. Absorption, reflection, refraction, transmittance, fluorescence, scattering, and resonance phenomena are studied by spectroscopy techniques. The spectral range for UV-Vis spectroscopy lies between 100 to 900 nm. The method is non-destructive, needs short analysis times, and is inexpensive [54]. For PVK characterization, absorption measurements as a function of the wavelength are commonly used to determine changes in absorption. The presence of absorption edges is typical for semiconductor systems and allow the identification of the band gap value [53].

- **Fabrication regime**

*Scanning Electron Microscopy (SEM)***:** This technique belongs to morphological characterizations and provides magnified images from a determined sample at a microscopic scale. Grain size, shape and composition is the type of information revealed by the scanning electron microscope. The technique consists of a finely focused electron beam that generates backscattered electrons and secondary electrons due to the beam interaction with the studied specimen [55]. SEM is applicable to characterizing the proposed fabrication procedure and validating PVK thin films' quality, i.e., uniformity, grain size, and roughness [53].

X-Ray Diffraction (XRD): This technique allows to evaluate crystallographic information through diffraction patterns. The substances absorb, transmit and diffract X-rays; every substance produces a characteristic diffraction pattern that depends on its crystal structure [56]. In the technique, crystalline materials are bombarded by a settled wavelength beam, and waves are scattered by the ion lattice generating a pattern [54]. Crystallinity is a relevant factor to validate PVK as a suitable material to develop solar cells. Crystallinity impacts the charge separation efficiency, change transport, and diffusion length, fundamental characteristics for photovoltaic applications [21]

2.6 Advances in perovskite thin films fabrication

To obtain high-quality PVK thin films several routes have been studied; optimizing the precursor solution preparation, changing PVK compositions, film processing techniques, and changes in the interface properties PVK-substrate [21]. Remarkable advances have been made regarding the composition of PVK films and new film processing procedures to develop reproducible, high-quality thin films [57], some of these advances are summarized as follows:

PVK Precursor solutions and composition advance.

- *Formamidinium (FA):* FA substitution in place A (from PVK structure ABX_3) has been shown to enhance the thermal stability of the PVK. Eperon and colleagues developed a method to incorporate FA into the perovskite structure and obtained PCEs up to 14%, while also partially introducing Br in the X site [58]. Experimentally, they used precursor solutions, spun coated on heated glass, and annealed at 170°C for 10 minutes to obtain uniform thin films [58]. In addition, FA advantages are related to a broad absorption range of the solar spectrum. Seok group also developed a method for producing dense and uniform high-quality thin films, with a PCE higher than 20%. A two-step methodology was employed; lead iodide dissolved in DMSO was spin-coated on top of the glass, followed by FAI dissolved in 2-propanol and annealed at 150°C for 20 minutes [38].

- *Thiocyanate:* Tai and colleagues worked with a *two-step* solution-processed method, using a precursor solution of $Pb(SCN)_2$ to partially dope with SCN in the I site. They showed that it is possible to reach PCE over 15% under non-controlled atmospheres with this substitution. Furthermore, the partial thiocyanate substitution results in better intrinsic stability than the pristine perovskite [24]. Sun et al. used $Pb(SCN)_2$ as an additive to the perovskite fabrication resulting in the increased crystallinity of the layer, defect-free perovskites, and long-life span of the thin film. The fabrication process was

carried out under non-controlled ambient conditions (room temperature and non-controlled atmosphere) [59].

- *Cesium doping:* Cesium doping was studied by Niu and colleagues. Working with the *one-step* solution-processed methods, they doped the perovskite with cesium to face the undesirable thermal instability of the perovskite layer. The thermal stability was proved under nitrogen and dry-air controlled atmospheres and a humid air non-controlled atmosphere resulting in superior thermal stability. It is significant that the thermal stability improves under specific cesium doping percentages and can optimize the thin-film morphology leading to higher device performance and a higher PCE. The device performance is better than the obtained for pure MA in the pristine perovskite [23]. Saliba et al. worked with triple cation systems, where partial substitutions into the A site were made with cesium and FA. Thus, the samples showed improved intrinsic thermal stability, reducing the phase impurities of the perovskite layer and building a perovskite with less sensitivity to the fabrication methods. The incorporation of Cs and FA results in defect-free perovskites, PCEs over 20%, and good reproducibility, a key factor for PCE manufacturing [37], [60]

- *Methylamine-based precursors:* CIDEMAT and Universidad de Antioquia, (Colombia) researchers have demonstrated that high MA rates induce complete solvation from PbI_6- inducing rapid crystallization and 3D α-phase purity. Experimentally, they proposed a viscous solution route that leads to photoactive PVK phases. It leaves PVK powder or crystals in a sealed vessel plus an amount of methylamine solution, promoting its diffusion and forming the viscous solution. Then, the viscous solution is deposited on the substrate surface by peeling or diluting it on organic solvents [61].

Film processing advances.

- *Preheating step:* Glass substrates are preheated on a hotplate before PVK deposition. Cheng and colleagues proposed this method. This simple step evaporates the absorbed moisture and oxygen from substrate and solvents employed, resulting in high-quality samples even on atmospheres exceeding 70% relative humidity [57].

- *Other synthesis routes:* Otálora and colleagues from Universidad Industrial de Santander, Universidad Nacional de Colombia, and Acádemicos por Colombia have proposed chemical bath deposition (CBD) resulting in grain sizes around 10 μm and high crystallinity. The method consists of a precursor solution containing lead iodide, MA, and γ-butyrolactone as solvent. Then, deposition is attained by dipping heated substrates into a saturated solution at 150°[62].

- *Antisolvent strategies.* In the one-step method the reaction time of all the components is short. On the other hand, solvents employed evaporate slowly. This time-scale difference leads to an uncontrolled morphology that can be minimized by the addition of antisolvents to the coating process. Taylor and colleagues proposed a methodology based on manipulating the antisolvent application rate. As a result, they obtained PVK solar cells with efficiencies >21%. Also, they highlight two key factors: 1) organic precursor solubility in antisolvents and 2) miscibility of the organic compound with the employed solvents [63]. On the other hand, Samadpour and colleagues modified antisolvent dripping, adding a small amount of tetraethyl orthosilicate into chlorobenzene, leading to high-quality PVK solar cells. These cells were stored and PCE decreased only 15% after 290 hours under ambient conditions [64].

2.7 Advances in perovskite stability

Several compositions and strategies have been implemented in high-performance PVK solar cells; compositional engineering is one of the keys to overcoming stability issues [65]. Some PVK layers with different cations are briefly described in **Table 1**, indicating initial and reduced PCE after fabrication. Some experimental details are also provided, including reagents in the precursor solution, solvents, antisolvents, additives, and some hole-transport materials employed.

***Table 1.** Stability breakthroughs. The table lists remarkable power conversion efficiencies (PCE) and device stability information. Experimental details are briefly described.*

Year	Perovskite layer	PCE %	Device stability	Experimental details
2016	$MAPb_{0.75}Sn_{0.25}(I_{0.4}Br_{0.4})_3$	12.6	After 720 h under an inert atmosphere, PCE reduced to 11.96%.	Precursor, one-step: PbI_2, $PbBr_2$, SnI_2, $SnBr_2$ and MAI Solvent: γ-butyrolactone: DMSO. Antisolvent: Toluene [66].
2016	$Cs_x(MA_{0.17}FA_{0.83})_{(100-X)}Pb(I_{0.83}Br_{0.17})_3$	>21	After 250 h under operational conditions, PCE reduced to ~18%.	Precursor one-step: FAI, PbI_2, MABr, CsI, and $PbBr_2$. Solvent: DMF: DMSO. Antisolvent: Chlorobenzene [37].
2017	$CsFAMAPbI_{3-x}Br_x$	>20	After 1000 h under illumination at 60°C, PCE reduced to ~19%.	Precursor one-step: FAI, PbI_2, MABr, CsI, and $PbBr_2$. Solvent: DMF: DMSO. Antisolvent: Chlorobenzene. They added a CuSCN layer on perovskite [67].
2017	$RbFA_{0.75}MA_{0.15}Cs_{0.1}PbI_2Br$	~16	After 12 h of continuous operation, PCE reduced to ~15.2%	Precursor one-step: $FAPbI_2$, $MAPbI_2Br$, $CsPbI_2Br$ MABr, and RbI. Solvent: DMF: DMSO and DMSO. Antisolvent: Chlorobenzene [68]
2018	$(FA_{0.76}MA_{0.21}Cs_{0.03})_{0.67}Pb(I_{0.89}Br)_{2.56}$	>18	After 1000 h under continuous, unencapsulated, ambient operation, PCE reduced to ~16.9%	Precursor one-step: FAI, PbI_2, MABr, CsI, and $PbBr_2$. Solvent: DMF: DMSO. Antisolvent: Chlorobenzene [69]
2018	$Rb_{0.05}Cs_{0.1}FAPbI_3$	20.3	After 1000 h under continuous	Precursor one-step: FAI, PbI_2, $RbPbI_3$, $FAPbI_3$ and

		operation, absolute PCE started at 18.74%, reduced to 17.51%	CsPbI$_3$. Solvent: DMF:DMSO. Antisolvent: Chlorobenzene [70]
2019	(FAPbI$_3$)$_{0.95}$(MAPbBr$_3$)$_{0.05}$	22.7	After 1370 h under 1-sun illumination at room temperature and continuous operation, PCE reduced to ~21.6	Precursor one-step: FAPbI$_3$, MAPbBr$_3$, and MACl. Solvent: DMF: DMSO. Antisolvent: Diethyl ether. Hole-transport material Poly(3-hexylthiophene) [71]
2019	FAPbI$_3$	23.5	After 1200 h, under constant AM 1.5G illumination without encapsulation, PCE reduced to ~21.13%	Precursor one-step: FAPbI$_3$ Solvent: DMF: DMSO. Antisolvent: Diethyl ether. MACl as additive [72]
2020	Cs$_{0.05}$FA$_{0.85}$MA$_{0.10}$Pb(I$_{0.97}$Br$_{0.03}$)$_3$	23.5	After 500 h under full-sun illumination and continuous operation, PCE reduced to ~22.3%	Precursor one-step: Solvent: FAI, PbI$_2$, MABr, and CsI. Solvent: DMF: DMSO. Antisolvent: Chlorobenzene [73]
2020	FAPbI$_3$	24.6	After 500 h under humid conditions (RH 50%), PCE reduced to ~21.44%	Precursor one-step: FAPbI$_3$ and MACl. Solvent: DMF: DMSO. Antisolvent: Diethyl ether [74]
2021	MAPbI$_3$	21.1	After 100 h under maximum power tracking conditions, PCE reduced to ~12.7%	Precursor one-step: (2-(2,3,4,5,6-pentafluorophenyl)ethylamonium), MAI, and PbI$_2$. Solvent: γ-butyrolactone:DMSO. Antisolvent: Toluene. 0.3 mol% salt was added. [75]
2021	(Cs$_{0.05}$(FA$_{0.83}$MA$_{0.17}$)$_{(0.95)}$Pb(I$_{0.83}$Br$_{0.17}$)$_3$)	21.0	After 720 h unencapsulated devices, stored in a nitrogen glove box, PCE reduced to ~16.8%	Precursor one-step: FAI, PbI$_2$, MABr, CsI, and PbBr$_2$ Solvent: DMF: DMSO. Antisolvent: Chlorobenzene. Additive dopamine [76]

2.8 Efficiency records

Efficiency records have been summarized in **Table 2**; these efficiencies have been certified by the NREL [16]. Authors, and a brief description of the fabrication procedure are exposed.

19

Table 2. *Perovskite solar cells efficiency records. Certified efficiency values have been summarized with a brief description of the fabrication method.*

Year	PCE%	Authors	Description
2009	3,8	Akihiro Kojima, Kenjiro Teshima, Yasuo Shirai, and Tsutomu Miyasaka [77].	The first solar cell (dye sensitizes liquid junction) with $CH_3NH_3PbBr_3$ and $CH_3NH_3PbI_3$ perovskites. Unstable perovskite
2012	9,7	Michael Grätzel and colleagues [78].	They developed PVK solar cells with a long-term duration with solid-state mesoscopic heterojunction.
2013	12,9	Burschka and colleagues [79].	The PVK solar cell was fabricated using sequential PbI_2 deposition, spin-coated on a TiO2 mesoporous surface. The method includes dipping in an MAI solution [2].
2014	16,2	Jeon and colleagues (Seok Group)	The PVK solar cell used the antisolvent method with the $MAPbI_3$ deposition on the TiO_2 mesoporous layer. The technique includes spin-coating [2].
2015	20,1	Yang and colleagues (Seok Group) [38].	The PVK solar cell was fabricated using the antisolvent method.
2016	21,6	Saliba and colleagues [37]	They developed a multiple cation strategy adding rubidium, cesium, and FA, MA to the perovskite with a two-step method and spin-coating.
2017	22, 1	Yang and colleagues [80].	The PVK solar cell was prepared using a substitution strategy and contains FA with multiple cations and mixed halide anions.
2018	23,7	Jeon and colleagues. (Korea Research Institute of Chemical Technology) [81].	Optimization of the HTL composition. They developed a fluorene-terminated hole-transporting material.
2019	25,2	Yoo and colleagues (Korea Research Institute of Chemical Technology/ MIT) [18].	The PVK solar cell with the highest record certified efficiency uses the antisolvent method and a passivating agent.

3. OBJECTIVES

3.1 General Objective

Develop hybrid lead halide perovskite thin films doped with cesium and thiocyanate by means of spin coating.

3.2 Specific Objectives

- Design and construct an acrylic glove box to prepare the precursor solutions and grow the perovskite thin films with relative humidity levels under 20%.
- Prepare hybrid lead halide perovskite thin films under controlled atmospheric conditions through the spin-coating method.
- Conduct partial ion substitution with cesium and thiocyanate on hybrid lead halide perovskite thin films.
- Determine structural and optical properties of hybrid lead halide perovskite thin films and their dependence on doping level and synthesis parameters.

4. METHODOLOGY

The methodology is summarized according to specific objectives from **Figure 7**. Every specific objective is matched with its corresponding activities. Each of the four specific objectives has been assigned two activities. These activities are detailed in the following sections.

1. Design and construct and acrylic glove-box to prepare the precursor solutions and grow the perovskite thin films with relative humidity levels under 20%.	• 1.1 Glove-box design and construction. • 1.2 Glove-box tuning.
2. Prepare hybrid lead halide perovskite thin films under controlled atmospheric conditions through the spin-coating method.	• 2.1 Precursor solution preparation. • 2.2 Fabrication of perovskite thin-films by spin-coating method.
3. Conduct partial ion substitutions with cesium and thiocyanate on hybrid lead halide perovskite thin films.	• 3.1 Substitutions on the A-site with cesium. • 3.2 Double perovskite susbtitution with cesium and thiocyanate.
4. Determine structural and optical properties of hybrid lead halide perovskite thin films and their dependence on doping level and synthesis parameters.	• 4.1 Characterize structural and optical properties. • 4.2 Data analysis for synthesis parameters and doping levels.

Figure 7. Methodology according to the four specific objectives. A list of two activities is assigned to each specific objective

4.1 Design and construct an acrylic glove box to prepare the precursor solutions and grow the perovskite thin films with relative humidity levels under 20%.

4.1.1 *Glove box design and construction.* PVK fabrication procedure was always carried out inside an acrylic glove box. The first stage of the project was the design and construction of the glove box, as depicted in **Figure 8** using Software Inventor (Autodesk, United States). The glove box was built-in transparent, not textured acrylic sheets with 10 mm thickness. Pieces were cut individually, using a computer numerical control (CNC) milling machine from Fablab laboratories at Universidad de La Sabana. The final stage was glove box assembling, mechanical joints were employed together with methylene chloride for soldering the acrylic sheets.

Electrical connections for glove box electricity supply were made through high-quality soldering. In addition, gas pipes (Pe al Pe), hoses, gas regulator devices, and gas flowmeter were installed and connected to an oil-lubricated vacuum pump and a nitrogen tank.
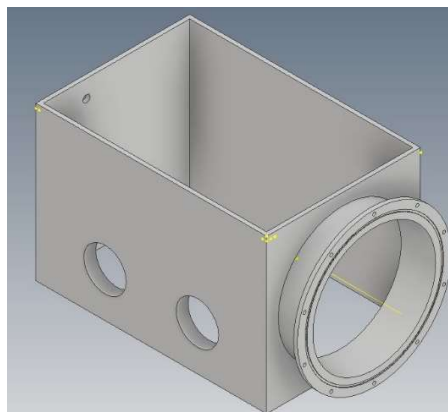
Figure 8. *Glove box primary draw. Essential representation from glove box on Inventor software 3D view.*

4.1.2 **Glove box tuning.** Subsequently, several vacuum leak tests were performed to confirm its hermeticity with diluted liquid soap. Soap foam was distributed evenly on glove box junctions. This technique allows for the visible detection of leaks by bubble emission due to pressure differences between the test part and the glove box inside (ASTM International, 2018). The tests were performed to determine the number of leaks, vacuum time, and relative humidity levels. Humidity data was measured with a hygrometer (Traceable, United States). After finding a leak, it was marked and immediately filled with epoxy adhesive. The leak filling was left to dry for at least 24 hours before performing a new leak test.

4.2   Prepare hybrid lead halide perovskite thin films under controlled atmospheric conditions through the spin-coating method.

4.2.1 *Precursor solution preparation. Pristine perovskite precursor solution.* Lead containing powder lead II iodide PbI_2 was purchased from Sigma-Aldrich (Missouri, United States) with a purity of 99.999%. Solvents N, N-Dimethylformamide anhydrous (DMF) with 99.8% purity and Dimethyl Sulfoxide anhydrous (DMSO) with 99.9% purity also were purchased from Sigma-Aldrich (Missouri, United States). Stock solution $S-PbI_2$ was prepared by heating PbI_2 powder on a hotplate for one

hour at 280°C. Then, the powder was mixed with solvents DMF: DMSO in a 4:1 proportion in volume and stirred overnight. Solution concentration was set and filtered on a 0.45 µm pore size, PTFE hydrophilic syringe filters (Thermo Scientific, China). S-PbI$_2$ density was determined by employing a linear regression on volume and mass measurement series obtained from 100 µL aliquots. Pristine PVK precursor solution S-MAPbI was prepared by mixing stock solution, as shown in **Figure 9**. Lead iodide solution S-PbI$_2$ was mixed with methylammonium iodide anhydrous powder (MAI), purchased from Sigma-Aldrich (Missouri, United States) with a purity of 99%. It was added to the S-MAPbI solution by inserting a stoichiometric powder amount.
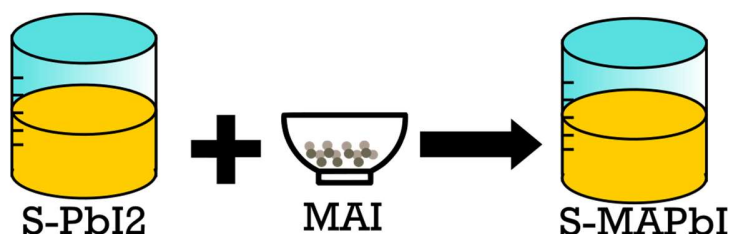
Figure 9. Pristine perovskite precursor solution. S.MAPbI solution is made by mixing lead iodide solution and adding a stoichiometric amount of MAI powder.

4.2.2 *Fabrication of perovskite thin films by the spin-coating method.* PVK thin-film deposition by the spin-coating method was carried out inside the homemade glove box filled with nitrogen and silica bed to minimize the relative humidity under 20% (the relative humidity at the laboratory was around 50-80%). Precursor solutions were prepared under a nitrogen atmosphere due to substances strongly reactant to moisture. PVK thin films manufacturing process was based on Saliba and colleagues method [60], Tai and colleagues method [24], and Cheng et al. method [57].

Figure 10 is a summary of the three giant steps that involve PVK fabrication. The technique consists of substrate cleaning, PVK precursor solution preparation, thin film deposition using spin coating, substrate preheating, and antisolvent addition.

Additionally, a complete list of the reactants used in the thin films fabrication is presented in **Table 17** from annexes.

1. Substrate cleaning	→	2. Perovskite Precursor Solution	→	3. Perovskite Film Deposition
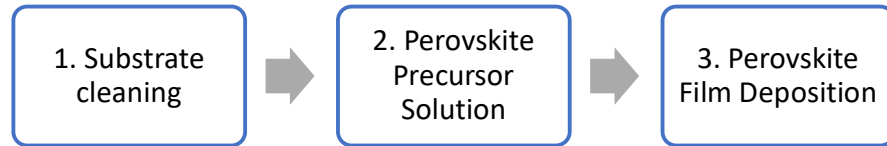
Figure 10. *Basic flowchart of the perovskite fabrication process. The perovskite fabrication followed the one-step Saliba et al. method* [60]. *It is grouped into three big steps substrate cleaning, perovskite precursor solution, and thin-film deposition.*

- ***Substrate cleaning.*** Fluorine-doped tin oxide (FTO) coated glass substrates with a nominal surface resistivity of 6 Ω/sq and 10mm x 10mm size were purchased from BIOTAIN Hong Kong Co (Fujian, China). Substrates were cleaned using a soft brush and Hellmanex (Hellma GmbH & Co. KG, Germany) mixed with deionized water (MolLabs, Colombia), 2:98 V:V. Next, substrates were cleaned using an ultrasound Transonic TI-H-10 (Elma Schmidbauer GmbH, Germany) for 15 minutes in Hellmanex bath and rinsed with deionized water at 80°C for 20 minutes. After that, an ultrasonic isopropanol bath was performed for 15 minutes. Subsequently, the substrate was rinsed with deionized water. Then, an ultrasonic bath in acetone was made for 15 minutes, followed by a rinse with acetone and afterward with isopropanol. Nitrogen and airflow were used to dry isopropanol. Finally, 15 minutes of UV-ozone treatment was performed in equipment from Ossila (Sheffield, United Kingdom).

- ***Water contact angle.*** Drops of distilled water were put on top of glass substrates, uncleaned, cleaned with Hellmanex, and washed with isopropanol and acetone, five samples for each cleaning procedure. The contact angle was determined using Mobile Drop equipment provided by Krüss Scientific

(Hamburg, Germany) and software Advance (Hamburg, Germany) included with the equipment.

- *Perovskite thin-film deposition.* **Figure 11** summarized deposition. Substrates were heated at 100°C for 4 minutes on a hotplate (Dlab Scientific, China). Then, the sample holder placed substrates on a spin coater provided by Ossila (Sheffield, United Kingdom). Following the one-step procedure and using a micropipette, a drop of precursor solution (35 µL) is deposited on the substrate center and spanned. Ten seconds before the end of the spin coater settled time, a drop of antisolvent (70 µL) is added, as shown in **Figure 11**. Two antisolvents were purchased from Sigma-Aldrich (Missouri, United States): chlorobenzene at 99.5% purity and 4-Tert-butylpiridene at 98% purity. The final step is annealing for a few minutes on a hotplate to induce all the precursors' reactions to form high quality and uniform PVK layer.
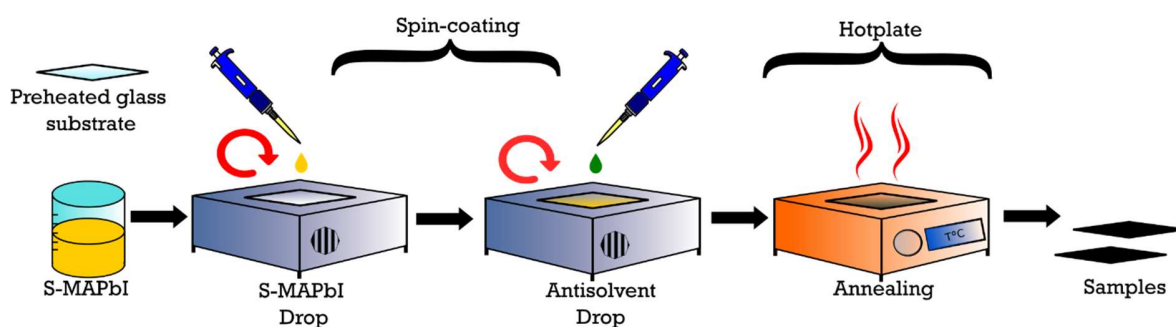
Figure 11. *Scheme of perovskite thin-film deposition. The fabrication of samples is based on the spin-coating technique and follows the one-step methodology. An additional antisolvent step is added before annealing in the hotplate.*

4.3 Conduct partial ion substitutions with cesium and thiocyanate on hybrid lead halide perovskite thin films.

4.3.1 *Partial substitutions on the A site of the perovskite with Cs.*

Cs doping PVK precursor solution. Cesium stock solution, S-CsI, was prepared by mixing cesium iodide, purchased from Sigma-Aldrich (Missouri, United States) at 99.999% purity, with DMF solvent with 1.5 molarity. Starting with pristine PVK

solution S-MAPbI as shown in **Figure 12**, a stoichiometric amount of S-CsI was added. The solution was labeled S-CsMAPbI, and its density was determined by weighting 100 µL aliquots and performing a linear regression. Cs doping content was ranged from 0% (control sample) to 20%.
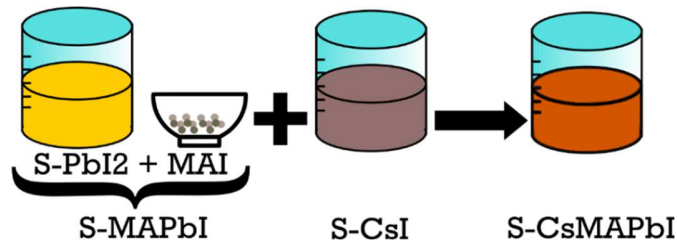
Figure 12. Cesium doped precursor solution. CsI stock solution (S-CsI) was mixed with pristine MAPBI3 solution (S-MAPbI) to get Cs doped perovskite precursor S-CsMAPbI.

4.3.2 *SCN and Cs doping PVK precursor solution.* A double doping precursor solution was prepared, as illustrated in **Figure 13**. First, lead-containing stock solutions S-PbI2 and S-PbSCN were a mix. Then, an amount of MAI powder was added and vigorously mixed. Finally, the S-CsI stock solution was added to obtain the S-CsMAPbSCNI PVK precursor solution.
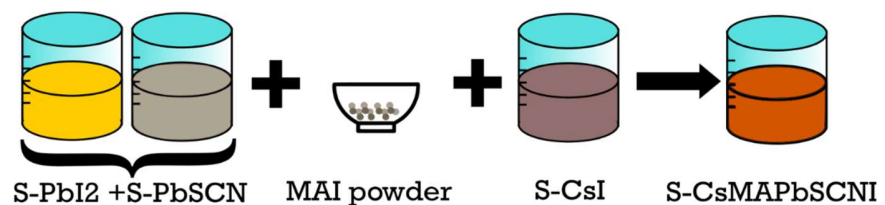
Figure 13. Double doping perovskite precursor solution. S-CsMAPbSCNI solution is prepared by mixing S-PbI2, S-PbSCN, MAI powder, and S-CsI.

4.4   Determine structural and optical properties of hybrid lead halide perovskite thin films and their dependence on doping level and synthesis parameters.

4.4.1 *Characterize structural and optical properties.*

- ***X-ray diffraction characterization.*** Structural properties were performed in an XPert Pro MPD X-ray diffractometer by Panalytical (Malvern, United Kingdom). All the samples were analyzed without further preparation. The two theta range was fixed to 10° to 90° with a step of 0.02° and 50s step time. Powder Cell software [82] was employed to analyze the sample diffraction patterns.

- ***SEM characterization.*** PVK thin-film samples were analyzed in a Phenom SEM (Thermo Fisher Scientific, United States) equipment. Sample preparation included painting a small point with silver paint acting as an electrode to ground the samples. Additionally, PVK samples were blown with compressed dry air to avoid contaminants. Top-view photographs were taken using a backscattered detector (BSD), Topo A, and Topo B detectors. The energy used was 10 000 kV.

- ***UV-VIS absorption spectroscopy characterization.*** UV-VIS absorption was performed in a UV-VIS spectrophotometer Evolution 201 Thermo Scientific (Massachusetts, United States). Samples were introduced on quartz cuvettes without further preparation to measure the absorbance. Cardboard sheets with a hole (4mm diameter) supported the samples inside the quartz cuvettes. The range was fixed from 500 nm to 900 nm for all samples, with a step of 1 nm. The integer time was set at 10 s.

4.4.2 *Data analysis*

- ***XRD.*** Powder Cell software [82] was employed to analyze samples XRD patterns. The Crystallographic Open Database (COD) was consulted online to obtain the reference patterns. The COD ID of the reference XRD patterns are listed in **Table 3**. XRD patterns data was normalized to stablish a comparison. The normalization consisted of dividing all the intensity points by the maximum intensity.

Table 3. X-ray diffraction patterns. COD ID, are listed for the five compounds of precursor solutions used as reference.

Compound	COD ID
Lead iodide, PbI_2	1011333
Cesium iodide, CsI	2106199
Methylammonium iodide, MAI	8000325
Lead thiocyanate, $Pb(SCN)_2$	2106398
Pristine PVK, $MAPbI_3$	7239521

- **Absorption.** A linear fitting in Python (Open Source), was used to determine the x-axis intercept of the absorption edge in the absorbance spectrum. Next, using the photon energy and wavelength relation presented in **Equation 1**, the energy band gap of the compounds were calculated.

$$E = \frac{hc}{\lambda}$$

Equation 1. Photon energy and Wavelength.

5. RESEARCH PRODUCTS

5.1 Papers submitted.

- Pending for submission.

5.2 Participation in academic events.

- Mónica López; *"Perovskitas para una nueva generación de celdas solares".* Virtual speaker. Encuentro Nacional de Estudiantes de Ingeniería Química y Procesos, ENEIQ 2020.

CHAPTER 1 THE GLOVE BOX

1.1 Overview

In this chapter we introduce the details of the design and fabrication of a glove box suitable for the synthesis of PVK thin films. Glove boxes are sealed containers designed to manipulate objects [83]. The box has orifices for gloves. These allow the user to handle materials and perform activities inside the isolated chamber preventing environmental contamination and controlling the atmosphere composition [84]. Employing glove boxes is an excellent alternative for handling sensitive materials, especially those incompatible with exposure to the standard ambient atmosphere [85]. Regarding PVK fabrication, it has been carried inside glove boxes since the very beginning of the research. Inherent lead toxicity, hygroscopic nature from reagents, and PVK sample degradation due to oxygen and moisture presence made compulsory working inside a glove box.

The effect of moisture on the formation of PVK thin films was studied by [86]. They prepared samples at different % of relative humidity (RH) : 0, 15, 30, and 45. They found that a small amount of moisture benefits PVK thin films' quality due to faster ion diffusion that induces PVK crystal growth and rapid crystallization. The beneficial effect is shown when not surpassing 45% RH and it is maximal around 15% RH. The fabricated glove box keeps RH levels under 20%, suitable for PVK thin films fabrication.

1.2 Glove box design

The design process followed the traditional inventor's approach consisting of recognition of need, the definition of the problem, synthesis, analysis, and evaluation [87]. Every stage will be further discussed in the following sections.

1.2.1 Recognition of need and definition of the problem: The hygroscopic nature of methylammonium iodide [88], lead iodide, and solvents toxicity [89] requires handling them inside a nitrogen atmosphere to reduce moisture and oxygen levels and prevent ambient contamination. The list of requirements and limitations associated with the design are presented and briefly explained in **Table 4**.

Table 4. Definition of the problem. The table contains the glove box fabrication requirements, and each one is briefly explained.

Requirement	Observations/details
Hermeticity	Hermetic door, mechanical and glue for sealing glove box junctions
Gloves	One pair of gloves. Two orifices
Transparent walls	Transparent non-textured acrylic sheets
Electrical supply	Three outlet plugs
Silica bed.	Two desks with small holes were on the glove box, creating space for a silica bed
Nitrogen atmosphere	Two valves
Relative humidity under 20%	Humidity is continuously measured with a hygrometer.
Shelves.	Three shelves were glued inside the glove box.
Dimensions	Dimensions length 80.2 cm, high 50.8 cm

1.2.2 Synthesis Glove box working system. The most common geometries used in the market for glove boxes are cubic-shaped with 90° between faces of the major body [83]. A 3D draw from the glove box is shown in **Figure 14**, and individual pieces are marked from **a)** to **f)**. Three box faces will include holes in our design: the frontal and its orifice (**Figure 14 A**), the laterals (**Figure 14 B**), and the back (**Figure 14 C**). The frontal hole is designed to put and take out the devices and supplies when needed. The lateral holes are for the gloves for the personnel that will manipulate

the apparatus inside the box. The back holes will let us connect the electrical devices with outside power connected by a metallic piece depicted in (**Figure 14 F**). These holes are designed to be circular since this type of geometry will reduce the concentration of stresses. Additionally, three groove geometries were carved on the frontal (**Figure 14 E**) and lateral holes for the O-Rings.
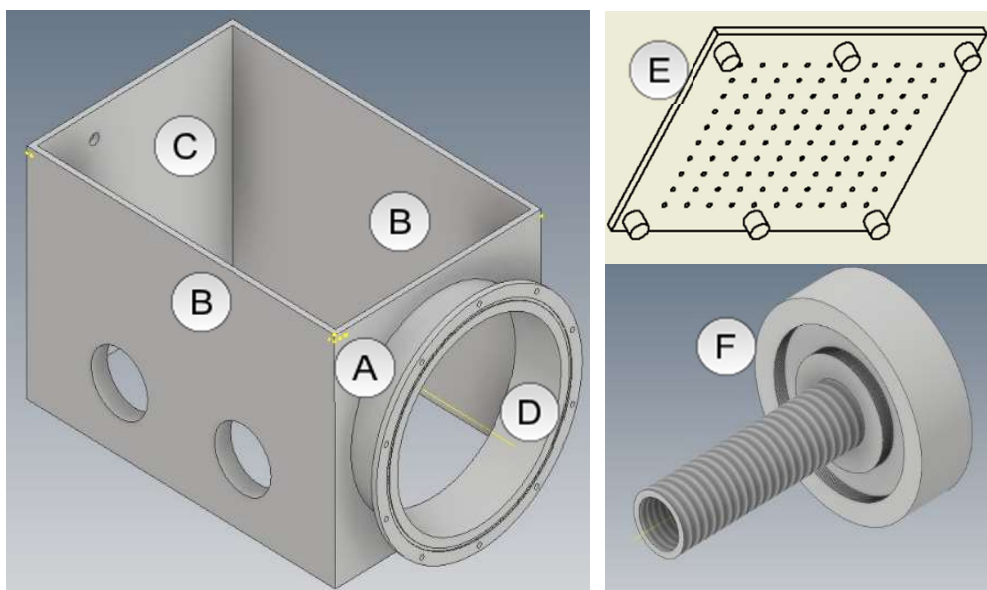
Figure 14. Glove box pieces. A-D) acrylic sheets, E) Table, and F) Electrical connections piece from stainless steel.

Figure 15 shows a schematic view from the glovebox. G-001 corresponds to the chamber, V-001 and V-002 correspond to gas valves, nitrogen tank is marked as C-001, and vacuum pump as P-001. The electrical connection is indicated as a box as well as the extraction process.
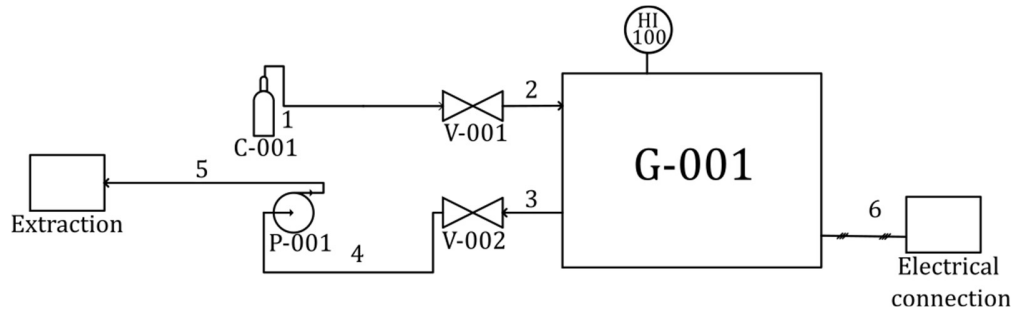
Figure 15. *Schematic view from the glove box. G-001 is the chamber, V-001 and V-002 are gas valves, HI 100 is a humidity sensor, C-001 is the nitrogen tank, and P-001 is the vacuum pump.*

1.2.3 Analysis

1.2.3.1 Analysis of forces. To validate the design, a simulation through FEA (Finite element Analysis) was executed in the Autodesk program, Inventor version 2020. **Figure 16 a)** shows the direction of the box's stresses when the vacuum is already created. For this simulation, it was considered that the pressure inside the box is 0 atm, and the stresses are inward and are due to atmospheric pressure, 1 atm.
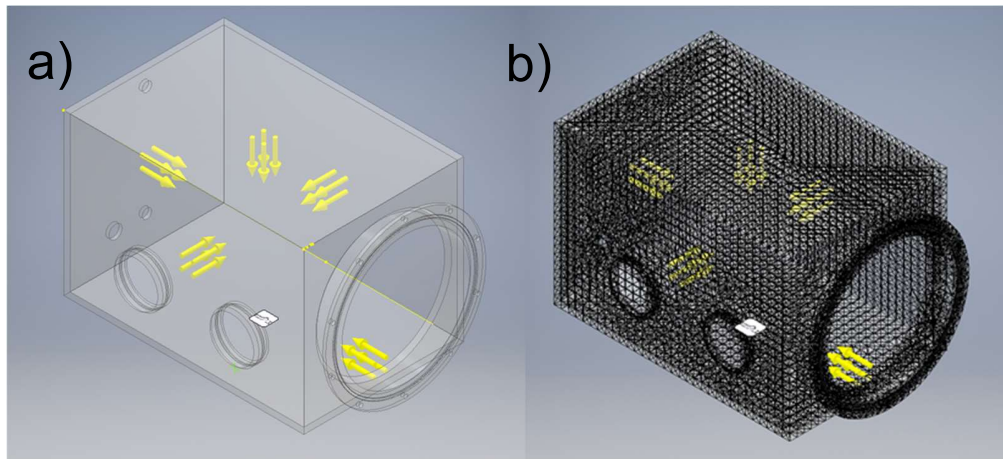
Figure 16. *a) Yellow arrows indicate the direction of the stresses applied to the box: each face is subjected to a 1atm stress. b) Meshing of the elements.*

The meshing of the elements and their result is shown in **Figure 16 b)**. The mesh setting for the simulation is reported in **Table 18** in the annexes. For this case, the areas where the box would be subjected to greater stresses were verified. Von Mises stress was calculated. It is a value used to determine if a given material will yield or fracture. This criterion is frequently used for ductile materials (metals). It specifies for a material that if the value of von Mises stress under load is equal or greater than the yield limit under simple tension, the material will yield [90]. **Figure 17** shows the result of the simulation. The maximum stress to which the box will be subjected has a value of 68.01 MPa and is located at the lower and upper sections of the lateral face. Although the glovebox works pefectly at normal conditions,according to simulation results bolts to join the faces were included; this added resistance to the critical zones found in the simulations.
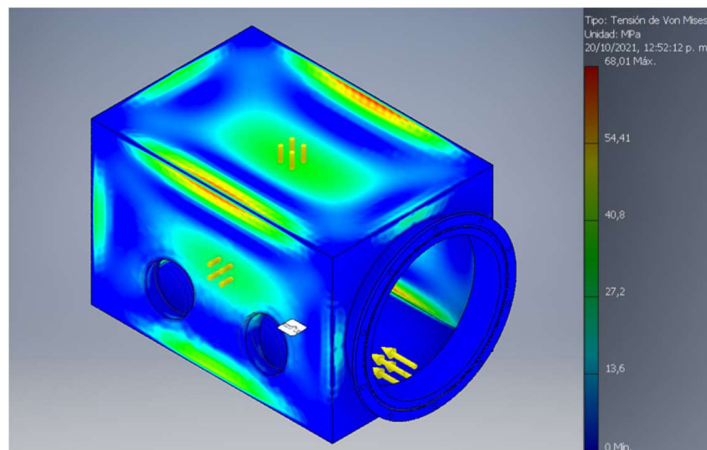
Figure 17. Von Mises stress results. The maximum stress sustained by the will be at the lower and upper section of the lateral face of the glovebox.

1.2.3.2   Selection of materials. The material selected for the glovebox was non-textured acrylic, which is inert and transparent, fulfilling the requirements from **Table 4**. The mechanical properties of the acrylic are shown in **Table 5** [91]. Also, three tensile tests were done at the Fablab facilities to verify the mechanical properties of the acrylic. Comparing the Von Mises stress test results and the value of the mechanical properties reported and obtained in the laboratory, it is lower than the

ultimate tensile stress and yield stress, making the material suitable for glovebox manufacturing.

Table 5. Physical and mechanical properties of acrylic. The properties are given in metric units.

Physical and mechanical properties	Metric units
Density	0.942-1.19 g/cc
Hardness, Rockwell M.	45-101
Ball indentation hardness	100-175 MPa
Tensile strength, ultimate	29-75 MPa
Tensile strength yield	44.9-86.0 MPa
Elongation at break	3.5-59%
Elongation at yield	4-6%
Modulus of elasticity	0.0420-3.30 GPa
Flexural yield strength	38-142 MPa

1.2.3.3   Detailed drawings. A detailed drawing was made using Autodesk Inventor for every glove box piece, which is depicted in **Figure 18**. The glovebox has six faces, frontal, back, two laterals, top, and bottom, forming the chamber. The frontal face with a cylinder with a removable lid fixed with bolts, as illustrated in **Figure 18**. The removable cover allows entering the equipment into the glovebox. Furthermore, two tables with holes were designed to work inside the chamber and are illustrated in **Figure 14 (E)**. Under the tables, a silica bed was placed.
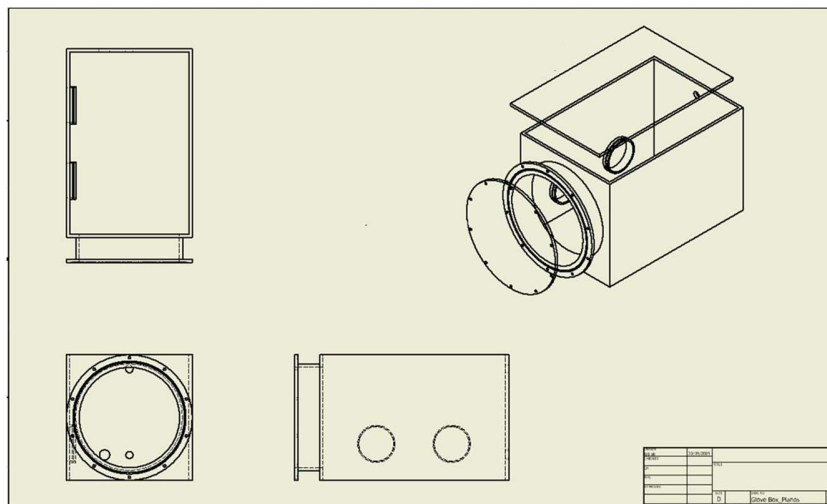
Figure 18. *Glove box detailed drawings. Several views from the glove box are illustrated frontal, isometric, and lateral views, respectively.*

1.3 Glove box assembly and tuning

1.3.1 Bubble test. The test is intended to detect and assess air leaks in the testing machine. It is quality control for the integrity of the devices tested [92]. The glove box was tested with an inexpensive bubble test. The results are reported in **Table 6.** Vacuum time was measured by filling the glove box with nitrogen. When the gloves fell because of nitrogen leaks, the time was taken. Relative humidity reached values around 2% after several trials and configurations of gloves, leakage coverage, and the addition of a silica bed.

Table 6. *Bubble test. Summary from the test performed. Leaks, vacuum time, and moisture were determined.*

Test Number	Number of leaks	Vacuum time (min)	% Moisture	Results
1	10	5	-	It could be seen that the camera had many leaks. Therefore, the empty time was going to be minimal.
2	6	6	-	There is an improvement in the number of leaks, and in the empty time, we proceed to continue covering the leaks found
3	4	5	-	There is an improvement in the number of leaks, and in the empty time, we proceed to continue covering the leaks found

4	3	4	-	A change in the gloves was made, and it is evident that the vacuum time is even shorter with fewer leaks than the previous test; the way the gloves are placed inside the chamber is corrected.
5	1	9	-	By correcting the position of the gloves and finding only one leak, it is evident that the vacuum time is better than in the previous tests
6	0	15	-	Having a longer vacuum time and not finding any leakage, we proceed to add Silica gel to absorb moisture and introduce the hygrometer
7	0	20	40	It is evident that the humidity can be improved, and the position of the gloves can be corrected again
8	0	20	30	There is an improvement in terms of % humidity
9	0	90	5	There is an improvement in terms of % humidity
10	0	90	2.1	Optimal working conditions

1.3.2 Assembled glovebox. The assembled glove box (chamber) is shown in **Figure 19 a)** and **b)** from different views. It was the first step of the assembling procedure. **c)** shows the electrical connections welded and designed to connect three plugs. **d)** exhibits the tables installed in place and the silica bed placed under them. **e)** and **(f)** show the fully assembled glovebox.

Additionally, bubble leak tests were performed regularly to assure the hermeticity of the chamber to maintain appropriate RH levels. The operating glove box is depicted in **Figure 20**. Three shelves were glued to the chamber walls to organize samples, reagents, and other instrumentation. To start working with the glove box, the two valves installed are open, a nitrogen flow enters the chamber, and at the same time, the vacuum pump extracts the gases inside the chamber. If the relative humidity levels exceed the established limit, the process is repeated, entering nitrogen and extracting the gas with the pump. This process lasts 10 to 15 minutes.
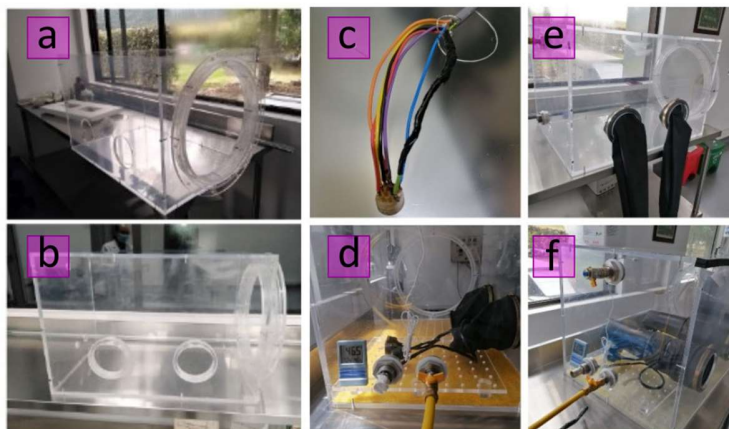
*Figure 19.*Assembled glove box. From (a-b) assembled chamber from different views, (c) electrical connections, (d-f) built glove box with silica bed, gloves, and valves.

Figure 20. Operating glove box. Three shelves were added to the glove box to organize reactants, samples, and instrumentation. The blue hose of the left enables nitrogen flow; the yellow hose allows pump extraction.

1.4 Conclusions

The designed and constructed glove box made in acrylic fulfilled all the requirements. It is hermetic, transparent, and has a pair of gloves. The electrical connections are functional, the tables allow the silica bed to be maintained, and the installed valves work correctly, permitting the flow of nitrogen and the pump

extraction process. The preparation of the glove box takes about 10 to 15 minutes before reaching an RH level under 20%, the low RH conditions are kept for about two hours. The installed shelves enable the organization of reactants, samples, and other instrumentation. The glove box allows an effective and safe manipulation of toxic and hygroscopic reagents, the preparation of precursor solutions, and the growing of PVK thin films.

CHAPTER 2 HYBRID LEAD HALIDE PEROVSKITES THIN FILMS AND SYNTHESIS PARAMETERS

2.1 Overview

In this chapter we present the results of the synthesis of pristine (methylammonium lead triiodide) PVK thin films by means of the spin-coating technique. Initially, substrate wettability was tested to ensure complete coverage at the deposition of the PVK precursor. Spin-coater velocity, annealing temperature, and antisolvent were the three factors evaluated to obtain the highest quality of films. The selected synthesis parameters will be used to synthesize the doped thin films.

2.1.1 Wettability. It is the tendency of the fluids to spread on or adhere to a solid surface surrounded by another fluid liquid or gas. Wettability can be measured through the contact angle at the liquid-solid surface as the angle decreases, the wetting tendency of the liquid increases. Complete wettability is evidenced by zero contact angle and Inversely 180° indicates a nonwetting preference [93].

2.1.2 Synthesis parameters. The spin coating technique is based on the equilibrium between centrifugal and viscous forces from the spinning and precursor solution. The angular velocity, also known as *spin-coater velocity,* impacts film thickness and, therefore, coverage. Typical spin coater velocities are around 300 and 10000 RPM and the spinning removes the excess from precursor solution and form the thin films [94]. An *antisolvent* is added to remove residual solvent from the wet samples [51]. Finally, the

thermal annealing dries solvent excess and allows crystal growth inside the thin-film. Solvent evaporation rate depends on solvent nature and ambient conditions. Non-uniformities in evaporation rate strongly affect thin film uniformity [50].

2.1.3 Bragg's law and interplanar spacing (d-spacing). XRD phenomenon is explained by the Braggs's law shown in **Equation 2**. This equation considers the wavelength, λ, the distance between two parallel planes, d_{hkl}, the diffraction angle for constructive interference, θ, and the other of the reflection n [95].

$$n\lambda = 2d_{hkl} \sin \theta$$

Equation 2. Bragg's law.

2.2 Precursor solutions and substrate cleaning

2.2.1 Precursor solutions. Two pristine PVK precursor solutions were prepared to evaluate the synthesis parameters. **Table 7** summarizes PbI_2 molarities and densities. Also, DMSO, and DMF densities were determined at 20°C. Fresh solutions were used to prepare all the samples PVK precursor solutions are colloidal. After several hours of aging, they exhibit incomplete PVK conversion and reduced device performance of solar cells. It is caused by the chemical inhomogeneity of the colloidal intermediates [96].

Table 7. Molarity and densities for solutions. Measured molarities and densities for PbI2 and solvents are reported. These were determined at 20°C.

Solution	Molarity (m/L)	Density (g/mL)
PbI_2 I	0.857	1.314(2)
PbI_2 II	1.060	1.369(1)
DMSO	-	1.22(1)
DMF: DMSO 4:1	-	0.9551(6)

2.2.2 Substrate cleaning. Wettability affects PVK precursor solution coverage on top of glass substrates. Two cleaning methods for substrate cleaning were tested, the contact angle technique was used to test their wettability. Uncleaned glass substrates were used as control. **Figure 21** shows the wettability tendency of the three substrates. **a)** corresponds to uncleaned substrates, **b)** cleaning method using isopropanol and acetone, and **c)** cleaning method using Hellmanex [60]. Evidently, cleaning only with isopropanol and acetone is insufficient to ensure proper wettability of the substrates and a contact angle similar to the one measured for uncleaned substrates is observed. After using Hellmanex, the drop spreads on the surface of the substrate and the contact angle becomes difficult to determine, which testifies to the large wettability of the substrate. All the samples studied in this thesis were prepared on top of Hellmanex processed substrates.
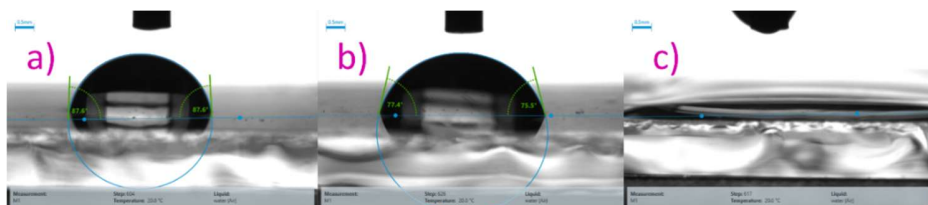
Figure 21. Contact angle photos. a) contact angle corresponding to uncleaned substrates, b) acetone and isopropanol cleaned substrates and c) Hellmanex cleaned substrates.

Table 8. Contact angle. Glass substrates were cleaned with two methods, adding Hellmanex, uncleaned, and washed with acetone and isopropanol. Hydrophilic and hydrophobic nature is indicated for every technique.

Cleaning method	Contact angle average (±9°)	Substrate Character
Uncleaned	84°	Hydrophobic
Acetone and isopropanol	76°	Hydrophobic
Hellmanex	Not determined*	Hydrophilic

Two deposition techniques were tested: slow and fast solution dropping. Complete coverage of the substrate was achieved with slow solution dropping and is depicted in **Figure 22**. This method was used to prepare all the PVK samples. The drop from slow dropping is distributed on the glass surface, in contrast with the fast deposition where the drop is applied to the center.
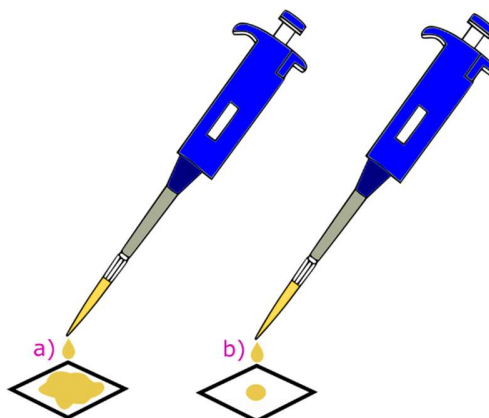
Figure 22. Solution dropping on top of glass substrate. a) Slow dropping, b) Fast dropping.

2.3 **Spin-coater velocity** and the impact on thin films morphology SEM characterization.

Four spin-coater velocities were initially studied: 3000, 4000, 5000, and 6000 RPM, respectively. The sequence programmed in the spin coater is illustrated in **Figure 23**, with a total length of 38 seconds. Small ramps in velocity were applied before the target velocity, which was kept for 20 seconds. All the parameters were fixed in the preparation of the thin films: same precursor solution, annealing time, annealing temperature, and the antisolvent.
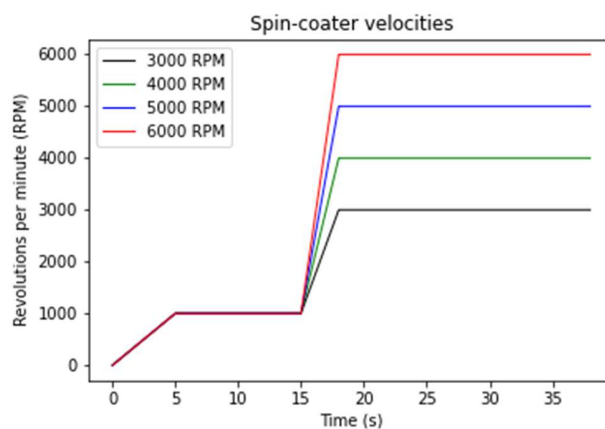
Figure 23. Spin-coater sequences. Four sequences with a total length of 38s were programmed, evaluating 3000, 4000, 5000 and 6000 RPM spin-coater velocities as target velocity.

To study the change in morphology caused by the different rotational speeds, SEM images were taken for all the samples, as shown in **Figure 24**. These images were obtained with the backscattered electron detector (BSD). For all coating speeds, the samples showed black spots corresponding to impurities and shown a needle-like granularity. However, samples coated at 4000 and 5000 RPM, showed fewer impurities on the thin film, a more uniform composition, and a better surface coverage.
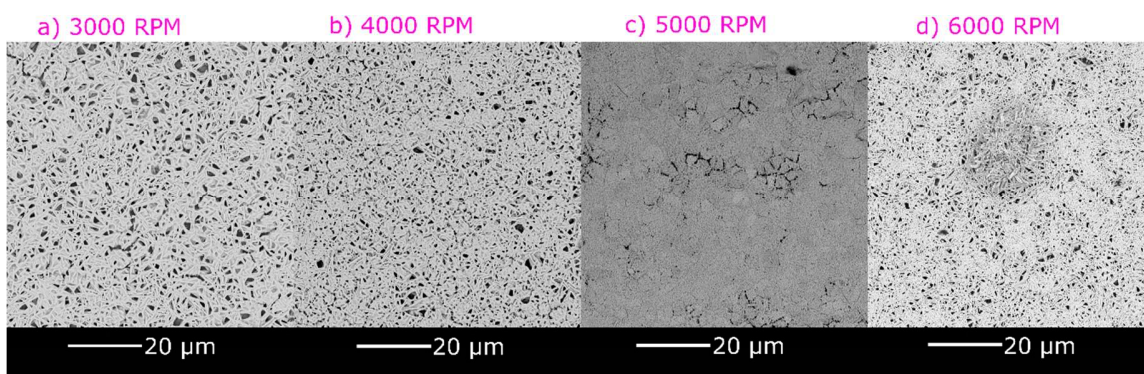
Figure 24. SEM images at different spin coater velocities. a) 3000 RPM, b) 4000 RPM, c) 5000 RPM and d) 6000 RPM. The white line is the scale bar corresponding to 20 μm. Images magnified at 3500x.

Subsequently, two sets of thin films were prepared at 4000 RPM and 5000 RPM spin-coater velocities, using annealing temperatures of 90 ºC, 100 ºC and 110 ºC. The SEM images of the samples are shown in **Figure 25**. Once again, in all cases we observe a needle-like structure with the presence of some impurities. However, the sample with the densest structure, and with the better visual characteristics was obtained under a spin coating speed of 4000 RPM. Topographic SEM images for samples prepared at 4000 RPM are shown at a microscopic scale **Figure 36** from annexes. They evidence that for samples annealed at 90 ºC and 100 ºC the surfaces are flat and compact, whereas at an annealing temperature of 110 ºC the roughness of the surface increases.
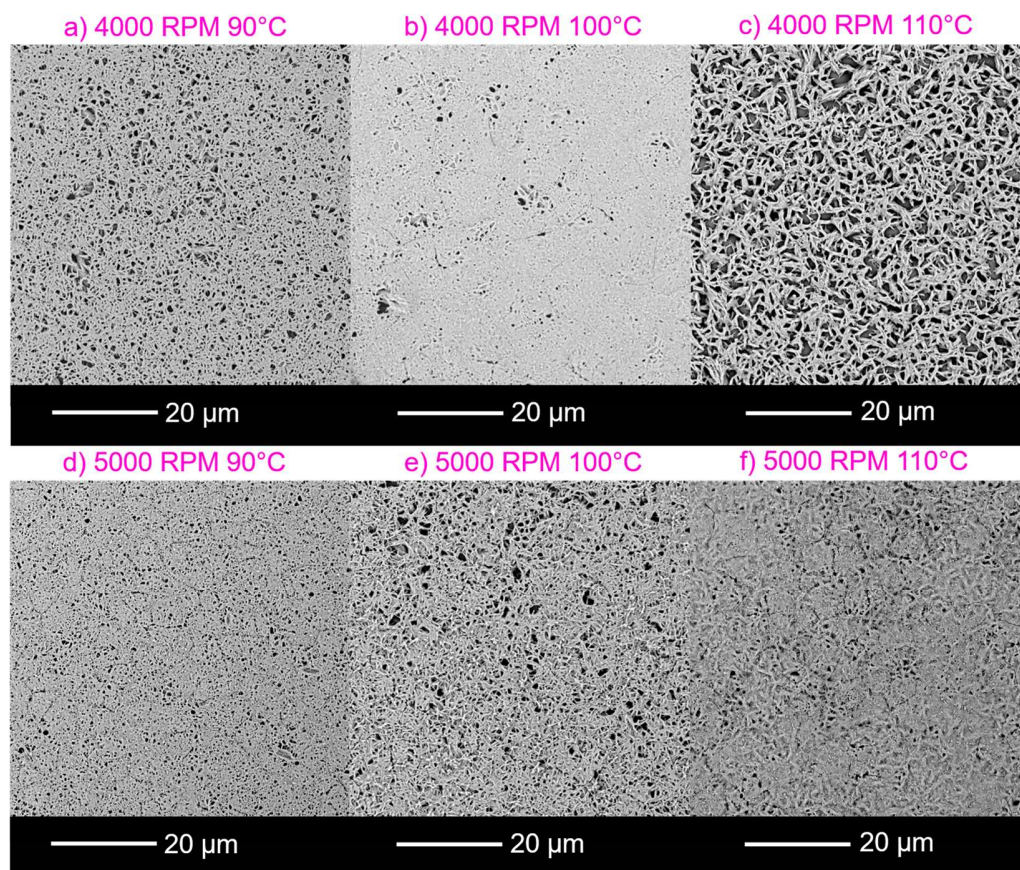
Figure 25. 4000 RPM and 5000 RPM SEM images. From a) to c) prepared samples at 4000 RPM. From d) to f) prepared samples at 5000 RPM. The white bar scale corresponds to 20 µm.

45

The selected spin-coater velocity according to SEM analysis is 4000 RPM due to the quality of the thin films compared to the other velocities tested. As suggested by Mehde and colleagues [97], the spin coating-velocity does not directly impact the morphology of samples, as evidenced in **Figure 25**. Angular velocities from spin-coating directly affect the thickness of the films, such as coverage [94], resulting in flatter and more compact PVK layers. The selected spin-coater velocity is also in concordance with the previous work reported by [62]. They prepared pristine PVK thin films under the one-step methodology with a rotational speed of 4000 RPM. Also, [97] prepared pristine PVK (MAPbI$_3$) samples using 4000 RPM as the spin-coater velocity.

2.4 Effect of the antisolvent on surface properties of PVK thin films.

Chlorobenzene is a typical antisolvent used in the preparation of PVK layers [64]. However, there are also reports of high-quality thin films prepared with a mixture of 4-tert-butylpyridine:chlorobenzene [98], [76]. Based on these results a comparison between both antisolvents the typical and the mixture was carried on. Two sets of samples were prepared at 4000 RPM at three annealing temperatures (90ºC, 100ºC and 110ºC) employing chlorobenzene and a mixture of 1:100 4-tert-butylpyridine: chlorobenzene. SEM images for the samples were taken and are depicted in **Figure 26**. As shown in panel **a)** the sample synthesized with chlorobenzene and an annealing temperature of 90ºC exhibits a compact and dense surface with no trace of impurities. Grains are not visible with the highest magnification of the SEM equipment at 27500x magnification, demonstrating that grains are at the submicron scale. As the annealing temperature increases, the samples show a needle-like structure that also increases in size.

SEM images for the 4-tert-butylpyridine samples are shown in **Figure 26 d) to f)** , in this case all the samples exhibit the needle-like pattern with the sample annealed at 100ºC exhibiting the denser and more compact film. Comparing the two sets of samples, films prepared using chlorobenzene and an annealing temperature of 90°C are the ones with the highest quality. Samples are compact, dense, smooth,

and flat. This observation is further confirmed by the topographic SEM images shown in **Figure 26 g) to j).** Chlorobenzene samples are generally smoother and denser than those prepared using the addition of 4-tert-butylpyridine. As a result, chlorobenzene has been chosen as the antisolvent for the synthesis of the doped films.
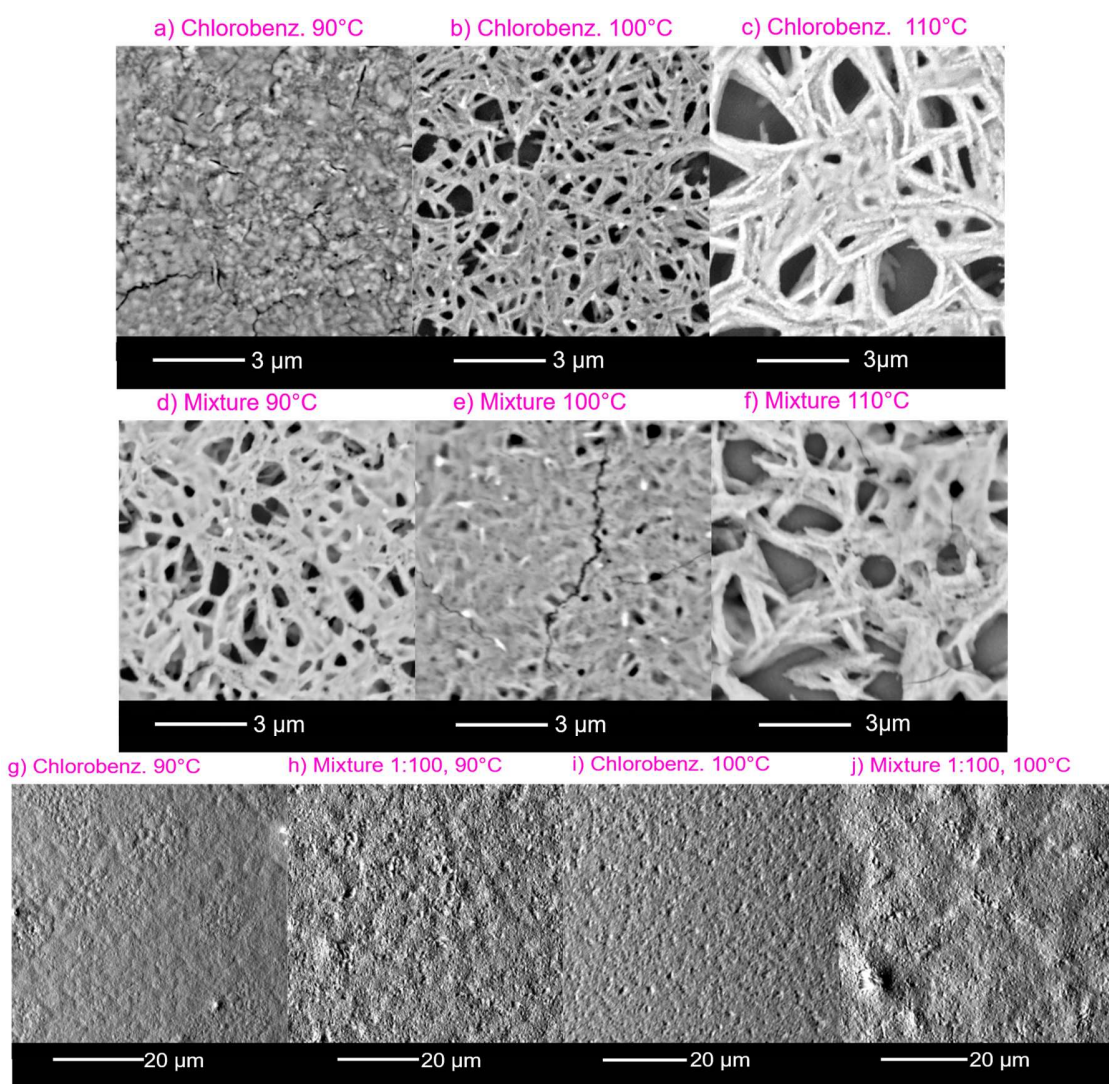
Figure 26. *Comparison of antisolvents. From a) to c) and d) to e), samples prepared with chlorobenzene and 4-tert-butylpyridine:chlorobenzene 1:100, respectively. The white bar corresponds to 3 μm. From g) to j) topographical SEM images, the white bar scale corresponds to 20 μm.*

Antisolvent plays a fundamental role in the quality of PVK layers and for most antisolvents there is a dependence on the antisolvent application time [63]. The application time of the chlorobenzene in the thin films was fixed at 5 seconds, which corresponds to a slow deposition. As suggested by [63], chlorobenzene is a type II antisolvent, implying that thin films' quality is irrespective of antisolvent application time. Previous works reported by [99], [100], and [59] obtained high-quality PVK layers with chlorobenzene as antisolvent.

2.5 Annealing temperature and the impact on PVK thin films structure

To define the working annealing temperature, thin films were prepared using 90ºC and 100ºC as the annealing temperature. The coating speed was fixed at 4000RPM, with chlorobenzene as antisolvent. At this stage, the PVK structure of the samples was tested by means of XRD diffraction studied.

The obtained XRD patterns are shown in **Figure 27**. The revealed peaks are characteristic from PVK compounds at around 14°, and 28° corresponding to the planes (110) and (220), respectively. These peaks are sharp and well defined, which suggest a good crystallinity for the films. The PVK layer prepared at 90°C, exhibits a cleaner pattern with sharper peaks than the patterns corresponding to the sample annealed at 100°C. Apart from a small peak at around 12.3º, which corresponds to the (001) plane of lead iodide, no other trace of impurities is observed in the sample annealed at 90ºC. In contrast, annealed samples at 100°C present peaks corresponding to MAI and lead iodide, evidencing incomplete conversion to the PVK phase. Together from this analysis and the previous SEM observations regarding the density and uniformity of the films, an annealing temperature of 90ºC was selected as the best option for the PVK thin films studied in this research.

The impact of the annealing temperature in PVK layers was previously studied by [101]. They suggest an optimum annealing temperature range between 80°C - 100°C. This range is concordance with the chosen annealing temperature of 90°C. They stated that annealing temperatures about 80°C do not fully convert the

precursor solution to the PVK phase, but after 120°C, PVK decomposes. Furthermore, it has been reported that the annealing step leads to the formation of a lead iodide and PVK mixed phase, with the annealing temperature determining the proportion between the two phases [102]. This effect is evidenced in the XRD patterns presented in **Figure 27**; after raising the annealing temperature, more impurities appear in the PVK layer. Moreover, the morphology is directly affected by changing the annealing temperature resulting in larger grain sizes as the temperature increases [101].

Interplanar distances (d-spacing) were calculated and reported in **Table 9** for PVK layers, according to XRD patterns. The d-spacing does not change significantly with the annealing temperature and it is in good agreement with previously reported values of is 6.2225 Å for pristine perovskite films [103].
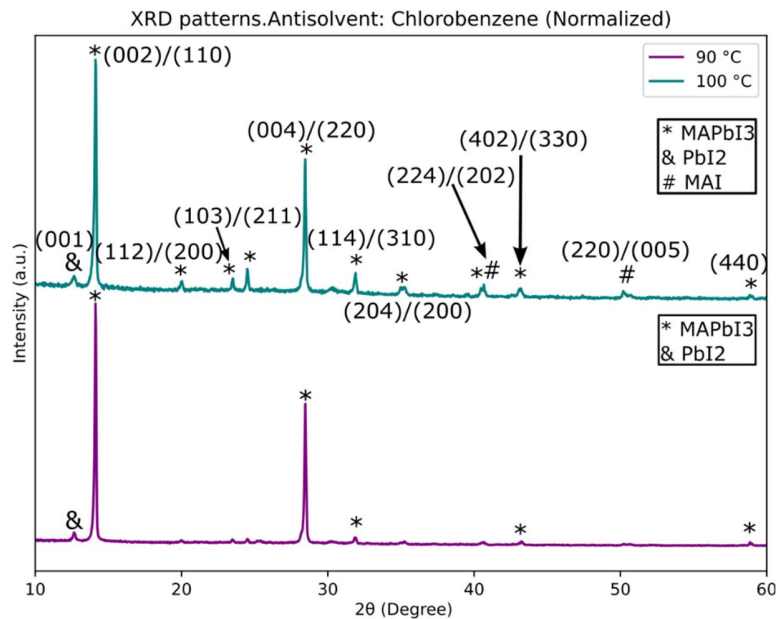
Figure 27. *XRD at different annealing temperatures. All the parameters were fixed, chlorobenzene was used as an antisolvent.*

The good quality of the films is further confirmed by the IR-VIS absorption measurement shown in **Figure 28**, which exhibits the expected behavior for the

pristine PVK. A large absorption is observed for wavelengths under 790 nm, belonging to the visible range of solar spectrum and a corresponding bandgap of 1.57 eV. This result is in concordance with the previously measured energy bandgap for pristine PVK films of 1.55 eV [104].

Table 9. *Lattice parameters calculations. Interplanar distances (d-spacing) at 90 °C and 100 °C*

Annealing T °C	d-spacing (Å)
90	6.273(4)
100	6.277
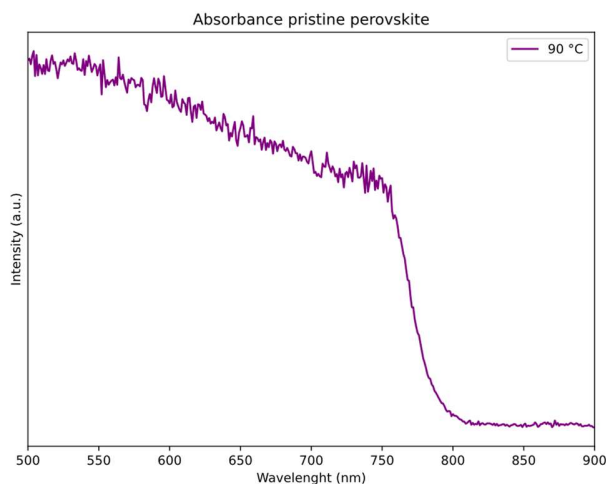
Figure 28. *Absorbance spectrum for pristine perovskite. Samples were annealed at 90°C. The absorption was measured in the range of 500nm to 900 nm. Absorption is given in arbitrary units.*

2.6 Conclusions

Several PVK layers were prepared to identify the synthesis parameters that obtain the highest quality of thin films. These were spin-coater velocity: 4000 RPM, antisolvent: chlorobenzene, and annealing temperature: 90°C. These parameters were chosen because the SEM images revealed a more uniform composition, similar structures along with the PVK layer, flat and dense surface of the film. Grains were not visible in the SEM images with a 27500x magnification (about 3 µm) because

they are at the submicron scale. The gap calculated for the pristine PVK layer is 1.57 eV. XRD patterns show good crystallinity and an almost pure perovskite phase with only a small proportion of lead iodide, no significant peak of MAI was found in the XRD patterns.

CHAPTER 3 CESIUM DOPED PEROVSKITE THIN FILMS

3.1 Overview

In this chapter we present the results of the Cesium doping on the A site of the PVK. Cesium doped PVK thin films were prepared aiming at three different doping levels 7%, 14%, and 20%. The samples were characterized morphologically by SEM images, XRD diffraction patterns and IR-VIS absorption to evaluate the inclusion of cesium in the PVK structure. Our results show that the inclusion of Cesium in the PVK structure is successful only up to a 7%.

The impact of doping in the A site of PVK concerns morphology and crystallinity, nucleation and growth, phase transition, and crystal orientation [105]. Regarding the influence on morphology, it has been shown that the pristine precursor solution mixed with cesium presents a higher solubility of lead iodide than the typical pristine precursor. It leads to PVK layers with bigger size grain than pristine thin films. Moreover, concerning the impact on nucleation and growth, the doping with cesium induces PVK seed at room temperature, which will further become nucleation sites promoting uniform grains as suggested by [100]. The control and reduction of nucleation sites during the growth of PVK crystals determine grain size. They are slowing the nucleation rate results in larger grains. Nevertheless, it also leads to pin-holes due to poor coverage [105]. The inclusion of cesium in the precursor solution slows down the nucleation rate, reflecting its improved thin-film uniformity.

3.2 Cesium series

3.2.1 Precursor solution. Fresh solutions were used to fabricate the PVK thin films. Molarities and densities are reported for stock solution lead iodide, cesium iodide, and precursor solutions are listed in **Table 10**.

Table 10. Molarity and densities for precursor solutions. Measured molarities and densities for PbI2, CsI, and precursor solutions are reported. These parameters were determined at 20°C.

Solution	Molarity (m/L)	Density (g/mL)
PbI$_2$	0.999	1.357(3)
CsI	0.999	-
Cs7%	-	1.40(1)
Cs14%	-	1.3613(3)
Cs20%	-	1.32(1)

3.2.2 Sample quality. Photos from the prepared samples and a description of their characteristics are presented in **Table 11**. To the eye, the sample with the best characteristics is the one corresponding to a 7% doping level, for which a uniform well covered sample is obtained.

Table 11. Annealing temperature summary of cesium doped thin films. Photos were taken from the prepared samples. Spin coater velocity was fixed at 4000 RPM. Cesium doping range from 7% to 20%.

Sample	Photo	Color	Observations
Cs 7%		Black and dark grey zones.	Uniformity: No, Translucent: No, Pinholes: No Coverage: Complete, Bright: Yes, Smooth: Yes

Cs 14%		Black and dark grey zones.	Uniformity: No. Translucent: No, Pinholes: No, Coverage: Complete, Bright: No, Smooth: No
Cs 20%		Black and dark grey zones.	Uniformity: No, Translucent: No, Pinholes: No, Coverage: Complete, Bright: No, Smooth: No
Cs 20% @ 100°C. *Annealing temperature 100°C		Brown and yellowish zones.	Uniformity: No, Translucent: No, Pinholes: No, Coverage: Complete, Bright: No, Smooth: No

3.2.3 SEM images. **Figure 29** presents SEM images for samples prepared at 90°C, increasing the doping level from 0% to 20%. From panels **a)** and **b)** in the Figure, it can be concluded that for the 0% and 7% cesium doping levels the films consist of a similar phase along the surface. There are no visible pinholes, demonstrating good coverage on top of the glass substrate. In contrast, for the 14% and 20% doping levels, depicted in panels **c)** and **d)** respectively, different structures on the PVK layer, corresponding to impurities, are evidenced. These structures are shown in more detail in panels **e)** to **h)** that present SEM images at 27500x magnification, where nail-shaped impurities can be identified. Surface information for the samples is illustrated in panels **i)** to **l)**. The smoother surfaces are observed for the pristine sample and 7% cesium doping levels. In contrast, the sample corresponding to a 20% cesium doping is largely rough.
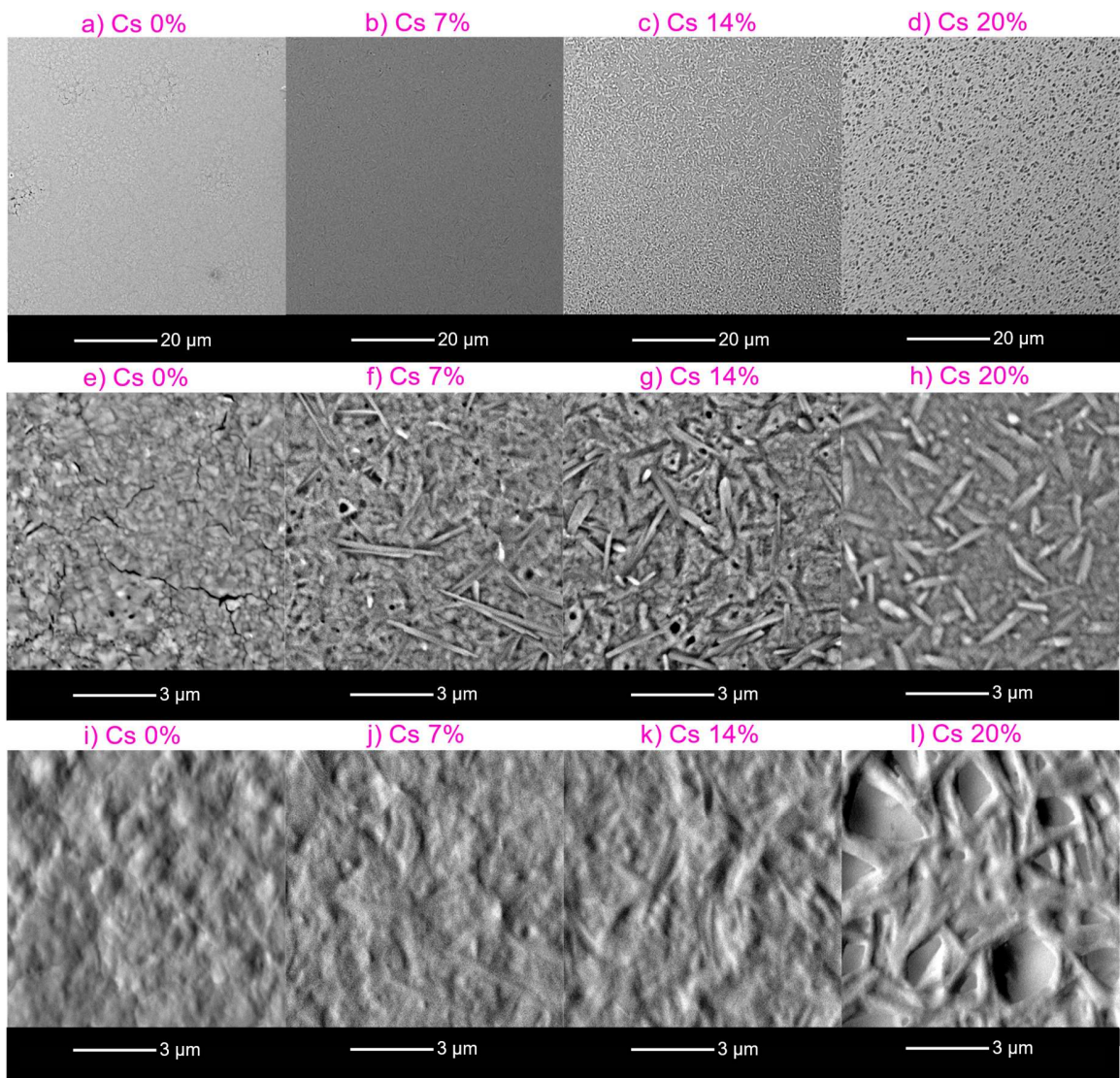
Figure 29. *Cesium series SEM images. From a) to d) white bar scale corresponds to 20 μm. From e) to l) white bar scale corresponds to 3 μm. From i) to l), SEM topological images.*

3.2.4 Crystallographic characterization. **Figure 30** shows the measured XRD patterns for the pristine PVK as the control sample and cesium doped thin films with a doping level from 7% to 20%. The formation of a PVK phase is confirmed by the clear appearance of the peaks at 14º, 28º, and 43º, corresponding to the crystal planes (002), (004), and (330), respectively. When comparing the control sample with Cesium 7%, no significant changes are observed in the peak's distribution,

neither for the PVK peaks nor the PbI2 ones. However, after a closer look, some new peaks in the doped thin films corresponding to MAI can be identified, such as the planes (200) and (202) at 40 and 40.4 degrees, respectively. These peaks, however, are barely visible, which suggests that the prevalence of impurities is largely negligible.
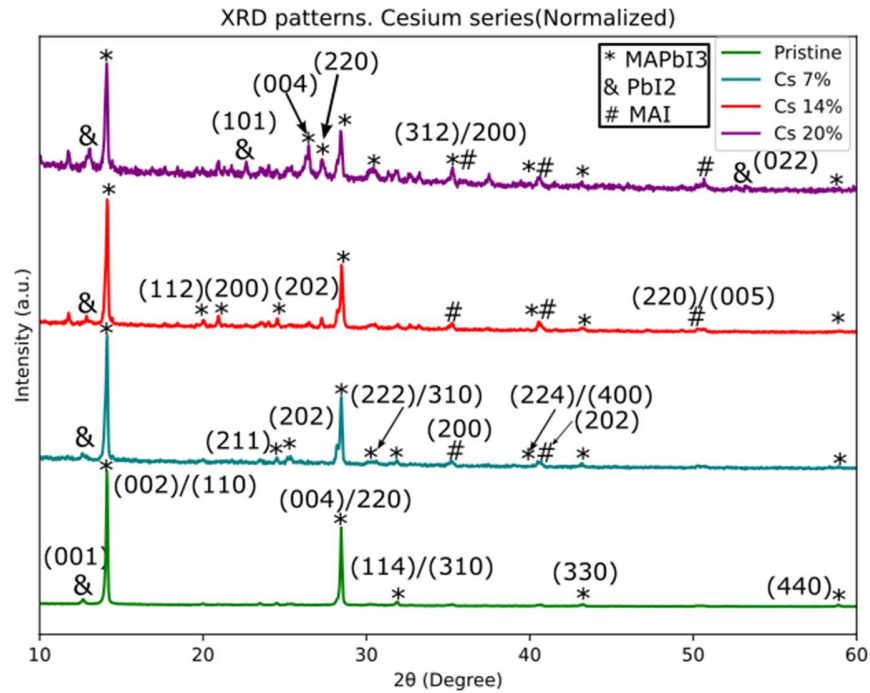
Figure 30. *XRD for cesium series. The parameters were fixed and prepared with three doping levels, 7, 14, and 20%. The green line represents the controls sample with no cesium doping.*

When the cesium doping level exceeds 7%, significant impurity peaks can be observed. For cesium 20%, additional peaks of lead iodide, such as (101) at 25.9° and (022) at 53.3°, can be identified. Besides, the lead iodide peak (001) is also more prominent. According to these XRD results, the Cs ions successfully incorporate into the perovskite structure only up to the 7% doping level. This result is in good agreement with recent works from [106] where it is stated that an improvement in the PVK layer is attained with Cs 5% doping level. The samples prepared by them had a dense and uniform morphology with full coverage.

56

Changes in PVK lattice parameters can be identified when there is a displacement in the XRD peaks. The family of planes [110] was used to determine their displacement and to calculate the interplanar distance (d-spacing) as the cesium doping level increases, the results are summarized in **Table 12**. According to d-spacing values, there is an essential difference between pristine (Cesium 0%) and Cesium 7% samples, further confirming the successful incorporation of Cs to the structure. For cesium 14% and 20%, the d-spacing magnitude decreases close to pristine PVK values, which suggest a lower incorporation of Cs into the structure. This is in good agreement with the observation of more and more intense impurity peaks as the cesium doping increases.

Table 12. . Interplanar distances for cesium doped samples. Pristine perovskite is added as a reference.

Cs doping %	d-spacing (Å)
0	6.273(4)
7	6.33(3)
14	6.31(3)
20	6.263(9)

To test the effect of the annealing temperature on the Cs incorporation, we grew another Cs 20% set of samples using an annealing temperature of 100ºC. The SEM images obtained for the two annealing temperatures with 20% cesium doping levels are depicted in **Figure 31** for comparison. More impurities and pinholes are indeed observed for the sample annealed at 90ºC, while the surface roughness seems to be similar for both annealing temperatures. This is in good agreement with recent studies where an annealing temperature of 100°C was chosen to obtain good quality films [37]. Nevertheless, the samples annealed at 100°C, decomposed after a few hours reaching the yellow phase characteristic of lead iodide.
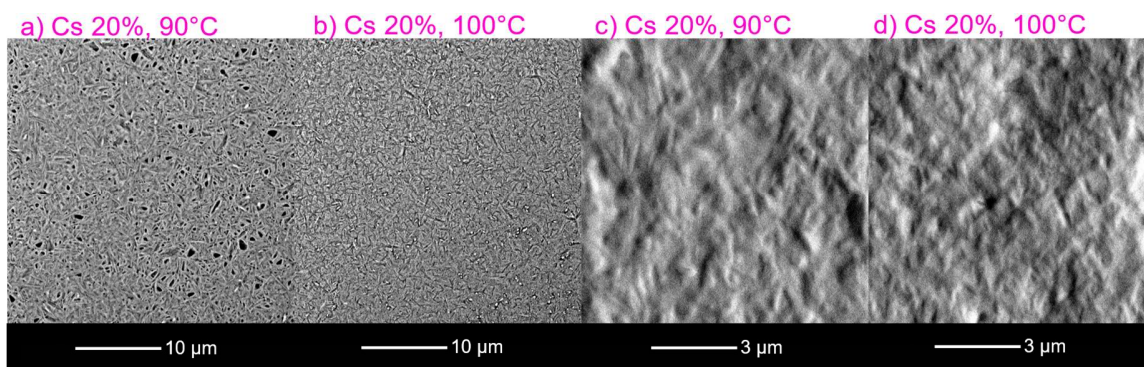
Figure 31. SEM images of cesium doped thin films. Samples are doped with 20% of cesium. a) and c) corresponds to samples annealed at 90°C. b) and d) correspond to samples annealed at 100°C. White bar scales indicate 10 µm and 3 µm, respectively.

2.1.1 IR-VIS absorption spectroscopy. **Figure 32** shows absorbance measurements for the cesium doped series and evidences the expected behavior for successfully cesium doped PVK layers; a blue-shift can be observed for the doped samples. This result is in good agreement with the results reported by [106], where a small blueshift in cesium-doped thin films compared to pristine PVK was reported.

Band gaps were calculated from the absorption spectra using first-order regressions, the results are reported in **Table 13**. The undoped pristine PVK control sample has a measured bandgap of 1.56 eV; after doping with cesium, the band gap increases to around 1.60 eV. This is clear evidence that cesium is incorporated effectively into the PVK structure. Nevertheless, the bandgap for all the cesium doping levels is almost constant, and slightly decreases at 20% cesium doping. This observation evidences that the changes in the PVK structure do not scale with the amount of cesium in the precursor solution, once more suggesting that after 7% no further cesium is introduced into the PVK structure. These results agree with the previous discussion on the interplanar distances (d-spacing) reported in **Table 12**. Although the ion in the A site does not directly impact the electrical properties of the PVK structure. It has a direct influence on the size of the unit cell and the atomic distances, thus inducing small changes in the bandgap [107].
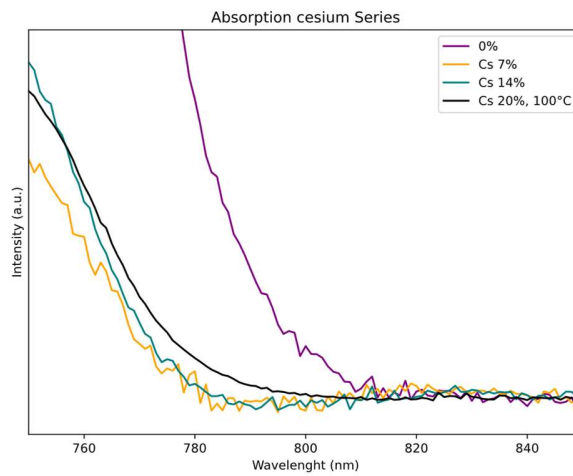
Figure 32. *Absorption cesium doped perovskite samples. Three levels of cesium doping are illustrated 7%, 14%, and 20% (Prepared at 100°C). Pristine perovskite spectrum is also added as the control sample and marked as Cs 0%.*

Table 13. *Cesium series measured band gaps. Band gaps for all samples are reported. Cs 0% corresponds to pristine perovskite used as the control sample.*

Sample	The measured band gap (eV)
Cs 0%	1.56
Cs 7%	1.60
Cs 14%	1.60
Cs 20%	1.59

3.3 Conclusions

In this chapter, we show our results regarding the Cs doping in the perovskite structure. Three different cesium doping levels were evaluated. The highest quality thin film was obtained at 7% cesium doping as evidenced in morphology from SEM images, where flat and compact thin films were obtained. Besides, the XRD patterns evidence that the incorporation of Cs is largely successful up to 7% doping level, for larger doping levels more and more intense impurity peaks can be observed.

59

Accordingly, the bandgap for the Cs-doped samples increases to 1.60 eV, from the 1.56 eV observed bandgap for the pristine structure. No significant dependence of the bandgap with the Cs content can be observed, which further confirms that the Cs incorporation in the perovskite structure is limited. After increasing the annealing temperature to 100ºC for a doping level of 20%, more uniform samples are obtained, however, these samples exhibited a fast decomposition into a yellow phase characteristic of PbI_2.

CHAPTER 4 DOUBLE DOPED PEROVSKITE THIN FILMS

3.1 Overview

In this chapter we present our results regarding our attempts to incorporate a double substitution of Cs and thiocyanate (SCN) in the A and X sites of the PVK structure, respectively. In all cases the cesium doping level has been fixed at 7%, which has been shown to exhibit a proper incorporation in the crystal structure. Thiocyanate doping levels were set at 7% and 14%. The characterization of the samples shows that, for the suggested synthesis procedure based on one-step coating, the inclusion of thiocyanate resulted in a minor conversion into the PVK structure and a fast degrading into a mostly amorphous phase.

It has been previously shown that the effect of doping in the X site of PVK with a pseudo halide, such as thiocyanate, is an increment in the bandgap as the concentration of the anion increases [108]. It is caused because the electrical properties of the PVK are associated to the B and X site. Additionally, studies performed by [25] suggested enhanced resistance to moisture of the PVK films after the thiocyanate insertion.

3.2 Precursor solutions

Information for PVK precursor solutions is reported in **Table 14.** Densities were determined at 20°C. Fresh solutions were used to prepare the samples. Molarity and densities for precursor solutions. Measured molarities and densities for precursor solutions are reported. These parameters were determined at 20°C.

Table 14. *Densities and molarities for precursor solutions. These values were estimated at 20°C*

Solution	Molarity (m/L)	Density (g/mL)
PbI$_2$	0.9737	1.299(8)
CsI	0.999	-
MAPbISCN (14%)	-	1.347(1)
MAPbISCN (20%)	-	1.278(9)

3.3 Sample characterizations

3.3.1 Sample quality. A brief description of the fabricated samples is included in **Table 15**. As shown, a few hours after the synthesis the samples exhibit a large transparency and a yellowish color, indicating a minor presence of the desired PVK phase.

Table 15. *Annealing temperature summary of double doped thin films. Photos were taken from the prepared samples. Spin coater velocity was fixed at 4000 RPM. Cesium doping is maintained at 7%, SCN level range from 7% to 20%.*

| Sample ID	Photo	Color	Observations
Cs 7, SCN 7		Dark brown, yellowish zones	Uniformity: No, Translucent: Yes, Pinholes: Yes, Coverage: Incomplete, Bright: No, Smooth: No
Cs 7, SCN 14		Dark brown, yellowish zones	Uniformity: No, Translucent: Yes, Pinholes: Yes, Coverage: Incomplete' Bright: No, Smooth: No
Cs 7, SCN 20		Dark brown, yellowish zones	Uniformity: No, Translucent: Yes; Pinholes: Yes, Coverage: Incomplete, Bright: No, Smooth: No

3.3.2 SEM characterization. The SEM images for the double doped PVK samples are depicted in SEM images in **Figure 33**. The 7% cesium doped sample was used as a reference and is presented in **Figure 33 a)**. It can be noticed that after introducing the thiocyanate content in the precursor solution, larger structures are present in the surface of the samples. When the thiocyanate doping level reaches 14%, the structure from the PVK layer becomes irregular, with visible pinholes that suggest an inadequate coverage on top of the FTO glass substrate.

The different structures of PVK layers are evident in 27500x magnified images illustrated in **Figure 33 d)** to **f)**. Pinholes, different phases, different grains orientation and structures are noticeable for the double-doped samples. Additionally, surface information for the thin films is presented from **g)** to **h)** the smoothest film corresponds to the control sample. The combination of cesium 7% and thiocyanate 14% consist mostly of a rough and porous PVK layer.

3.3.3 X-Ray diffraction. The results of XRD measurements are shown in **Figure 34** for all the samples. The XRD measurements were performed several hours after the annealing step, after reaching the yellow phase, because of the fast decomposition of the samples. The blue pattern is the reference sample cesium doped (7%), red and purple patterns correspond to double doped samples. The XRD patterns were compared with crystallographic information from lead iodide, lead thiocyanate, cesium iodide and pristine PVK, as indicated in section 4.4.2 of methodology.

XRD patterns purple and red present four prominent peaks at the positions of planes (001), (101), (003), and (004) of lead iodide. The other peaks correspond to phases of MAI and lead thiocyanate. Most of the present peaks in both patterns are not sharp or well defined. Together with the observation of a large background contribution, this observation suggests that the samples are largely amorphous. The pattern corresponding to a 7% thiocyanate (SCN) doping presents two peaks at the same position of the planes (004) and (220) of PVK compounds. Nevertheless, this is not a confirmation of the existence of a residual PVK phase because these peaks

are not well defined, and there are no more characteristic PVK peaks. These results are in concordance with the poor quality of the layers found in SEM images with different structures, a mixture of phases, and several pinholes.
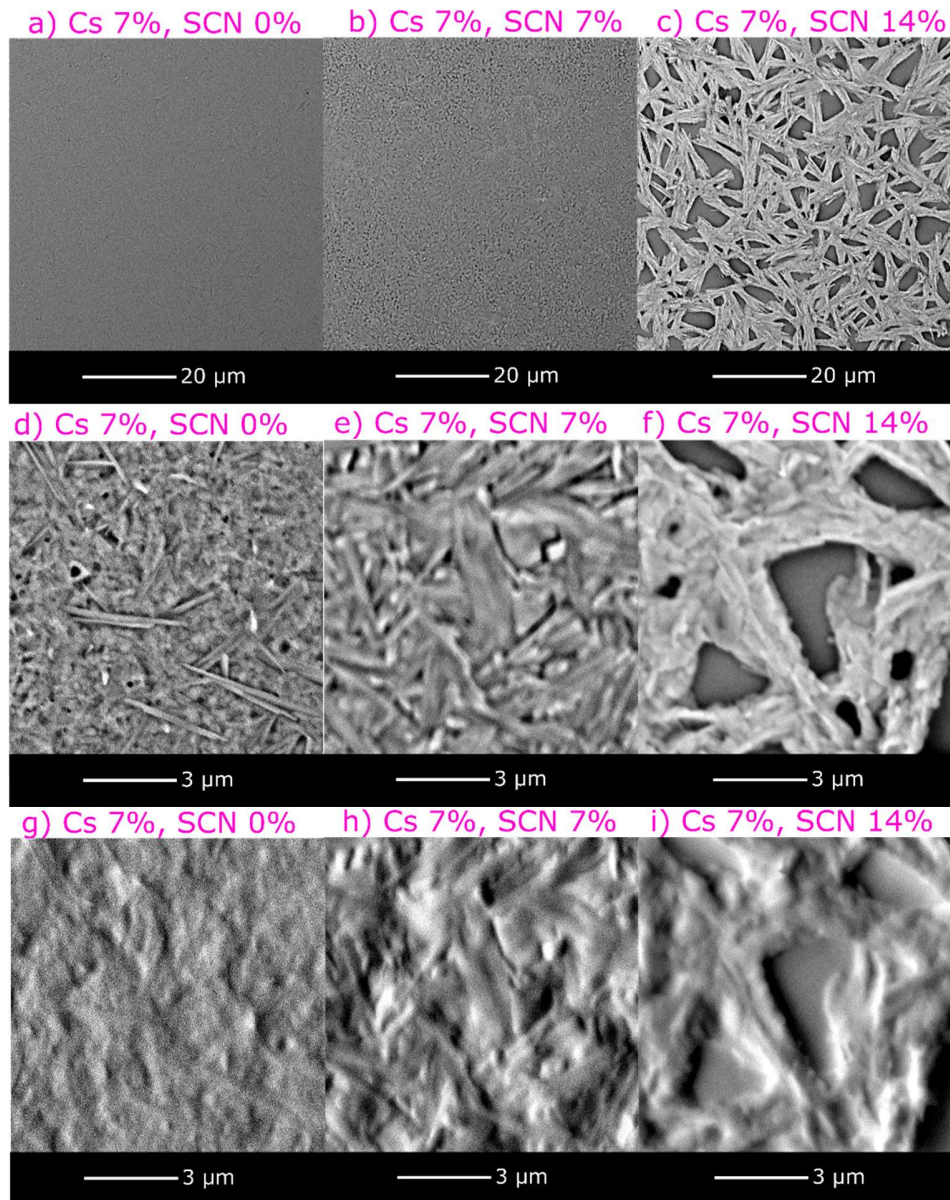
Figure 33. SEM images double doped series. From a) to f the white bar scale corresponds to 20 µm. From d) to i) the white bar scale corresponds to 3 µm. g) to i) topological images of the samples.
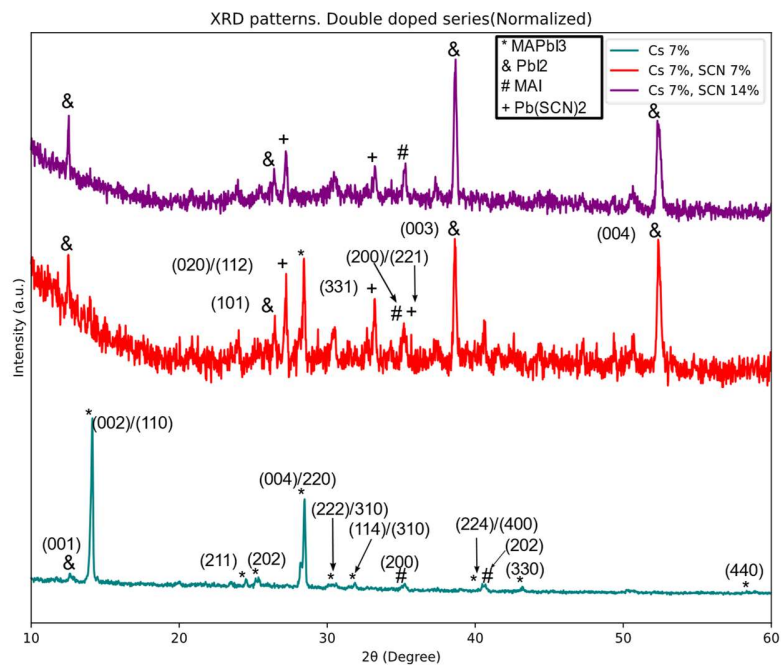
Figure 34. *Double doped XRD patterns. The blue line corresponds to reference perovskite doped with cesium 7%. Red and purple lines belong to double-doped samples.*

3.3.4 UV-VIS absorption spectroscopy. Double doped samples at different doping levels were characterized with absorbance measurements in the spectral range of 750nm to 850nm. The spectra are presented in **Figure 35**. The purple line corresponds cesium doped at 7% and annealed at 90°C, which is the reference sample. Green and blue lines correspond to double doped samples cesium 7%, thiocyanate 7% and cesium 7%, thiocyanate 14%, annealed at 90°C. These measurements were taken right after the preparation of the samples, before reaching the yellow phase.
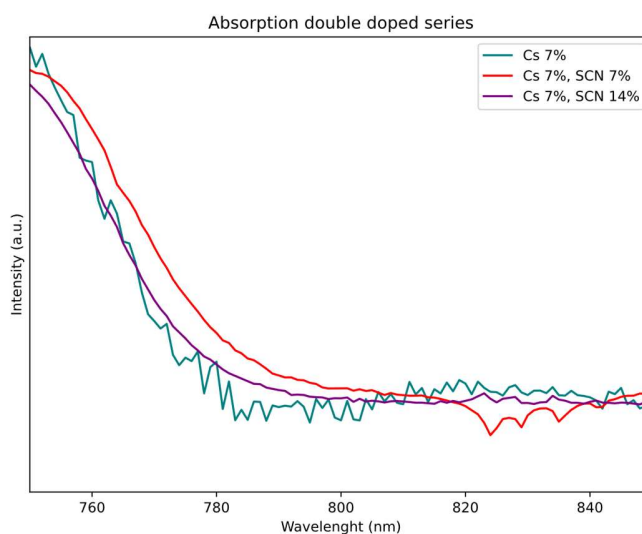
Figure 35. *Absorption spectra for double-doped perovskite samples. The purple line belongs to the control sample doped with Cs 7%, green and blue line corresponds to Cs 7%, SCN 7% and Cs7%, SCN 14%, respectively.*

Samples present evidence of a band gap characterized by an absorption edge around 760 nm. Band gaps for all samples were calculated with a linear fitting and the results are summarized in **Table 16**. As can be noticed, Band gaps do not present a significant change in magnitude despite the doping in the X site of the PVK and remain close to the estimated band gap of the reference sample. The band gaps thus suggest that there is not a significant insertion of thiocyanate into the structure [109].

Although the proposed one-step method brings the advantage of controlling the exact amount of dopants in the fabricated layers, it was not suitable to synthesize the desired double-doped PVK phase. The pseudo halide anions were previously reported as the dopant in the X site of the PVK by [24] through the spin coating technique. Tai and coworkers prepared PVK samples with enhanced moisture resistance based on a modified two-step deposition technique. The method consists of the formation of two layers. The first one is lead thiocyanate based followed by MAI solution. The second layer was repeated three times to assure the conversion

to the PVK phase. The doping level is unknown due to the nature of the method employed in the fabrication.

Table 16. Measured band gaps for the cesium and thiocyanate doped series. Cs 7% is reported as the control sample.

Sample	The measured band gap (eV)
Cs 7%	1.60
Cs 7%, SCN 7%	1.58
Cs 7%, SCN 14%	1.59

3.4 Conclusions

Double doped samples were prepared, keeping the cesium doping level fixed at 7%; the SEM images demonstrated a poor quality of the samples with poor coverage. The samples with thiocyanate exhibited a fast decomposition into a transparent yellowish phase that, according to XRD patterns, is composed of the precursor materials in a largely amorphous configuration. The estimated bandgap from absorption measurements carried out soon after the synthesis of the samples suggests that the thiocyanate does not incorporate into the PVK structure. The one-step methodology is not suitable to obtain the double doped PVK phase with partial and simultaneous incorporation of Cs in the A site and thiocyanate in the X site.

CONCLUSIONS

An acrylic glovebox was designed and fabricated. The glove box kept the relative humidity levels under 20%. Nitrogen supply and extraction through the vacuum pump worked appropriately, allowing to reduce the humidity levels in about 10 to 15 minutes. The glove box is suitable for the fabrication of perovskite thin films.

Pristine PVK layers were prepared through the one-step spin-coating methodology. The spin-coating velocity, antisolvent and the annealing temperature yielding the best quality PVK thin films were identified. Samples were characterized through SEM, XRD and IR-VIS absorption spectroscopy. SEM indicated that thin films were compact, flat, with the grain size at the submicron scale. XRD patterns revealed characteristic PVK peaks, with a minor presence of impurities. Absorption measurements exhibited the typical behavior of the pristine PVK, with a clear absorption edge and a corresponding bandgap of 1.56 eV.

Cesium doped layers were synthesized and characterized as the pristine layers. Champion thin films were obtained at a 7% level of doping. SEM images depicted a flat and compact layer, with grain sizes at the submicron scale. X-ray diffraction patterns evidenced characteristic perovskite peaks and presence of some impurities that become more pronounced for 14% and 20% doping levels. Changes in the calculated d-spacing indicate the insertion of cesium in the PVK lattice, which is further confirmed by a change in the calculated bandgap to 1.60 eV. However, these changes do not scale with the nominal cesium doping, which suggest that the effective cesium insertion in the PVK structure is limited to 7%.

Cesium and thiocyanate doped PVK films were deposited maintaining the cesium doping level at 7%. After the thiocyanate doping, the films exhibit a fast decomposition into a yellowish and transparent phase that, according to XRD results, is composed of the precursor components in a largely amorphous configuration. In agreement with this observation, SEM images showed poor quality thin films, with grains oriented in different directions and a mixture of phases along the layer. Absorption measurements indicated no significant change in the bandgap upon inclusion of thiocyanate, which indicates no insertion of thiocyanate in the perovskite lattice. The implemented one-step spin-coating methodology is therefore not suitable to achieve the desired double substitution in the perovskite layers.

RECOMMENDATIONS AND PERSPECTIVES

We have found evidence that there is a significant impact of the annealing temperature on the morphology and stability of the cesium doped films, further studies about the doping level and the annealing temperature will pave the way for better compositional engineering of PVK thin films.

Pseudo halide anions could be inserted in the PVK lattice through other deposition techniques, as the two-step methodology or dip coating. Further, exploration of these synthesis routes could result in a successful insertion of thiocyanate in the perovskite lattice.

ANNEXES

1. Materials for perovskite fabrication

*Table 17. Materials for perovskite fabrication. List of chemical substances. *Reactants employed for doped precursor solution.*

Step	Chemical/short formula	Name
Substrate cleaning	C_3H_8O	Isopropanol
	C_3H_6O	Acetone
	---	Hellmanex® III
Pristine perovskite precursor solutions	MAI	Methylammonium Iodide
	PbI_2	Lead iodide
	DMF	Dimethylformamide
	DMSO	Dimethylsulfoxide
*Perovskite precursor doped solutions	*CsI	Cesium iodide
	*$PbSCN_2$	Lead thiocyanate
Thin-film deposition	C_6H_5Cl	Chlorobenzene
	$C_9H_{13}N$	4-Tert-butylpiridine

2. Chapter one the glove box

Table 18. Mesh settings. For the simulation these parameters were fixed.

Setting	Value
Average element size	0.100
Minimum element size	0.200
Grading factor	1.500
Maximum turn angle	60.00 gr
Nodes	74686
Elements	37520

3. Chapter two synthesis parameters
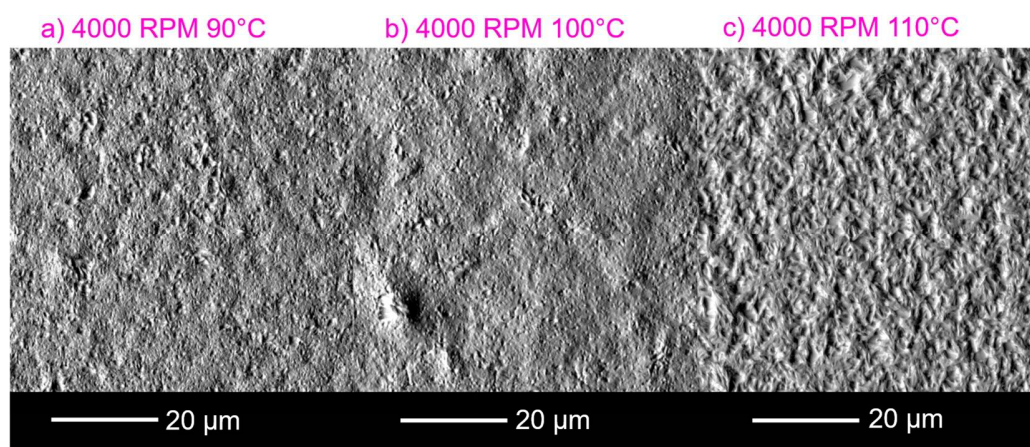
Figure 36. *Annealing temperature at 4000 RPM Topo A images. a) 90°C, b) 100°C, and c) 110°C. Pristine perovskite with fixed parameters, annealing time 5 min. Topo A detector.*

BIBLIOGRAPHY

[1] Z. Song *et al.*, "A technoeconomic analysis of perovskite solar module manufacturing with low-cost materials and techniques," *Energy Environ. Sci.*, vol. 10, no. 6, pp. 1297–1305, 2017, doi: 10.1039/c7ee00757d.

[2] J. P. Correa-Baena *et al.*, "The rapid evolution of highly efficient perovskite solar cells," *Energy Environ. Sci.*, vol. 10, no. 3, pp. 710–727, 2017, doi: 10.1039/c6ee03397k.

[3] IAEA, "Energy, electricity and nuclear power estimates for the period up to 2050," 2017.

[4] IEA, "2018 World Energy Outlook - Executive Summary," *Oecd/Iea*, p. 11, 2018, [Online]. Available: www.iea.org/t&c/.

[5] E. Papadis and G. Tsatsaronis, "Challenges in the decarbonization of the energy sector," *Energy*, vol. 205, p. 118025, 2020, doi: 10.1016/j.energy.2020.118025.

[6] United Nations, "Ensure access to affordable, reliable, sustainable and modern energy," *Sustainable Development Goals*, 2019. https://www.un.org/sustainabledevelopment/energy/ (accessed Sep. 15, 2019).

[7] B. Chen, R. Xiong, H. Li, Q. Sun, and J. Yang, "Pathways for sustainable energy transition," *J. Clean. Prod.*, vol. 228, pp. 1564–1571, 2019, doi: 10.1016/j.jclepro.2019.04.372.

[8] N. Kannan and D. Vakeesan, "Solar energy for future world: - A review," *Renew. Sustain. Energy Rev.*, vol. 62, pp. 1092–1105, 2016, doi: 10.1016/j.rser.2016.05.022.

[9] T. Ibn-Mohammed *et al.*, "Perovskite solar cells: An integrated hybrid lifecycle assessment and review in comparison with other photovoltaic technologies," *Renew. Sustain. Energy Rev.*, vol. 80, no. June, pp. 1321–1344, 2017, doi:

10.1016/j.rser.2017.05.095.

[10] P. G. V. Sampaio and M. O. A. González, "Photovoltaic solar energy: Conceptual framework," *Renew. Sustain. Energy Rev.*, vol. 74, no. June 2016, pp. 590–601, 2017, doi: 10.1016/j.rser.2017.02.081.

[11] S. A. Olaleru, J. K. Kirui, D. Wamwangi, K. T. Roro, and B. Mwakikunga, "Perovskite solar cells: The new epoch in photovoltaics," *Sol. Energy*, vol. 196, no. July 2019, pp. 295–309, 2020, doi: 10.1016/j.solener.2019.12.025.

[12] A. Acevedo-luna, R. Bernal-correa, J. Montes-monsalve, and A. Morales-acevedo, "Design of thin film solar cells based on a unified simple analytical model," *Rev. Mex. Trastor. Aliment.*, vol. 15, no. 6, pp. 599–608, 2017, doi: 10.1016/j.jart.2017.08.002.

[13] N. A. Ludin *et al.*, "Prospects of life cycle assessment of renewable energy from solar photovoltaic technologies: A review," *Renew. Sustain. Energy Rev.*, vol. 96, no. April, pp. 11–28, 2018, doi: 10.1016/j.rser.2018.07.048.

[14] L. Meng and J. You, "Addressing the stability issue of perovskite solar cells for commercial applications," *Nat. Commun.*, pp. 1–4, 2018, doi: 10.1038/s41467-018-07255-1.

[15] K. Mertens, *Photovoltaics : fundamentals, technology and practice*. 2014.

[16] National Renewable Energy Laboratory, "Best research cell efficiencies," *NREL Transforming Energy Photovoltaics Research*, 2020. https://www.nrel.gov/pv/cell-efficiency.html.

[17] Nature, "A decade of perovskite photovoltaics," *Nat. Energy*, vol. 4, no. 1, p. 1, 2019, doi: 10.1038/s41560-018-0323-9.

[18] J. J. Yoo *et al.*, "An interface stabilized perovskite solar cell with high stabilized efficiency and low voltage loss," *Energy Environ. Sci.*, vol. 12, no. 7, pp. 2192–2199, 2019, doi: 10.1039/c9ee00751b.

[19] S. He, L. Qiu, L. K. Ono, and Y. Qi, "How far are we from attaining 10-year lifetime for metal halide perovskite solar cells?," *Mater. Sci. Eng. R Reports*, vol. 140, no. January, p. 100545, 2020, doi: 10.1016/j.mser.2020.100545.

[20] R. Wang, M. Mujahid, Y. Duan, Z. K. Wang, J. Xue, and Y. Yang, "A Review of Perovskites Solar Cell Stability," *Advanced Functional Materials*, vol. 29, no. 47. pp. 1–25, 2019, doi: 10.1002/adfm.201808843.

[21] K. P. Bhandari and R. J. Ellingson, *An Overview of Hybrid Organic–Inorganic Metal Halide Perovskite Solar Cells*. Elsevier Inc., 2018.

[22] F. Bella, P. Renzi, C. Cavallo, and C. Gerbaldi, "Caesium for Perovskite Solar Cells: An Overview," *Chem. - A Eur. J.*, vol. 24, no. 47, pp. 12183–12205, 2018, doi: 10.1002/chem.201801096.

[23] G. Niu, W. Li, J. Li, X. Liang, and L. Wang, "Enhancement of thermal stability for perovskite solar cells through cesium doping," *RSC Adv.*, vol. 7, no. 28, pp. 17473–17479, 2017, doi: 10.1039/c6ra28501e.

[24] Q. Tai *et al.*, "Efficient and stable perovskite solar cells prepared in ambient air irrespective of the humidity," *Nat. Commun.*, vol. 7, pp. 1–8, 2016, doi: 10.1038/ncomms11105.

[25] A. Bahtiar, M. Putri, E. S. Nurazizah, Risdiana, and Y. Furukawa, "Environmentally stable perovskite film for active material of high stability solid state solar cells," *J. Phys. Conf. Ser.*, vol. 1013, no. 1, 2018, doi: 10.1088/1742-6596/1013/1/012176.

[26] M. Saliba, "Polyelemental, Multicomponent Perovskite Semiconductor Libraries through Combinatorial Screening," *Adv. Energy Mater.*, vol. 9, no. 25, pp. 1–8, 2019, doi: 10.1002/aenm.201803754.

[27] United Nations, "Paris Agreement," *United Nations*. 2015.

[28] A. Malhotra and T. S. Schmidt, "Accelerating Low-Carbon Innovation," *Joule*, vol. 4, no. 11, pp. 2259–2267, 2020, doi: 10.1016/j.joule.2020.09.004.

[29]   X. Chen, M. B. Mcelroy, Q. Wu, Y. Shu, and Y. Xue, "Transition towards higher penetration of renewables: an overview of interlinked technical, environmental and socio-economic challenges," *J. Mod. Power Syst. Clean Energy*, vol. 7, no. 1, pp. 1–8, 2019, doi: 10.1007/s40565-018-0438-9.

[30]   International Energy Agency (IEA), "IEA PVPS Annual Report 2019 Photovoltaic Power Systems Programme," 2019.

[31]   Banco Interamericano de Desarrollo *et al.*, "Proyectos Transformacionales Región Andina," 2020.

[32]   Minenergía, "ABC Construyendo la hoja de ruta de la energía del futuro," 2020.   [Online].   Available: https://www.minenergia.gov.co/documents/10192/24169616/ABC+Misión+Tr ansformación+Energética.pdf.

[33]   DNP Departamento Nacional de Planeación, L. Alberto, D. Gómez, A. García, D. Ríos, and O. Romero, "Informe anual de avance en la implementación de los   ODS   en   Colombia,"   2020.   [Online].   Available: https://www.ods.gov.co/es/resources.

[34]   DNP Departamento Nacional de Planeación, "Agenda 2030 in Colombia," *DNP   Departamento   Nacional   de   Planeación*,   2021. https://www.ods.gov.co/en/goals/affordable-and-clean-energy.

[35]   Congreso de la República, *Law 1715 of 2014*. Colombia, 2014.

[36]   Ministerio de Minas y Energía, Gobierno de Colombia, I. D. Duque Márquez, D. Mesa Puyo, M. Lotero Robledo, and S. Sandoval Valderrama, "Transición energética : Un legado para el presente y el futuro de Colombia," 2021.

[37]   M. Saliba *et al.*, "Cesium-containing triple cation perovskite solar cells: Improved stability, reproducibility and high efficiency," *Energy Environ. Sci.*, vol. 9, no. 6, pp. 1989–1997, 2016, doi: 10.1039/c5ee03874j.

[38]   W. S. Yang *et al.*, "High-performance photovoltaic perovskite layers fabricated

through intramolecular exchange," *Science (80-.).*, vol. 348, no. 6240, pp. 1234–1237, 2015, doi: 10.1126/science.aaa9272.

[39] K. Wang, D. Yang, C. Wu, M. Sanghadasa, and S. Priya, "Recent progress in fundamental understanding of halide perovskite semiconductors," *Prog. Mater. Sci.*, vol. 106, no. June 2018, p. 100580, 2019, doi: 10.1016/j.pmatsci.2019.100580.

[40] Y. Yan, W. J. Yin, T. Shi, W. Meng, and C. Feng, *Organic-Inorganic Halide Perovskite Photovoltaics: From Fundamentals to Device Architectures*. 2016.

[41] M. Habibi, F. Zabihi, M. R. Ahmadian-Yazdi, and M. Eslamian, "Progress in emerging solution-processed thin film solar cells - Part II: Perovskite solar cells," *Renew. Sustain. Energy Rev.*, vol. 62, pp. 1012–1031, 2016, doi: 10.1016/j.rser.2016.05.042.

[42] M. Righetto *et al.*, "Coupling halide perovskites with different materials: From doping to nanocomposites, beyond photovoltaics," *Prog. Mater. Sci.*, vol. 110, no. August 2019, p. 100639, 2020, doi: 10.1016/j.pmatsci.2020.100639.

[43] N. Marinova, S. Valero, and J. L. Delgado, "Organic and perovskite solar cells: Working principles, materials and interfaces," *J. Colloid Interface Sci.*, vol. 488, no. November, pp. 373–389, 2017, doi: 10.1016/j.jcis.2016.11.021.

[44] X. Zhao, D. Yang, J. Ren, Y. Sun, Z. Xiao, and L. Zhang, "Rational Design of Halide Double Perovskites for Optoelectronic Applications," *Joule*, vol. 2, no. 9, pp. 1662–1673, 2018, doi: 10.1016/j.joule.2018.06.017.

[45] M. K. Assadi, S. Bakhoda, R. Saidur, and H. Hanaei, "Recent progress in perovskite solar cells," *Renew. Sustain. Energy Rev.*, vol. 81, no. May 2017, pp. 2812–2822, 2018, doi: 10.1016/j.rser.2017.06.088.

[46] Y. Cheng, F. So, and S.-W. Tsang, "Progress in air-processed perovskite solar cells: from crystallization to photovoltaic performance," *Mater. Horizons*, 2019, doi: 10.1039/c9mh00325h.

[47] Y. Huang *et al.*, "Towards Simplifying the Device Structure of High-Performance Perovskite Solar Cells," *Adv. Funct. Mater.*, vol. 30, no. 28, pp. 1–16, 2020, doi: 10.1002/adfm.202000863.

[48] P. Nam-Gyu, M. Grätzel, and T. Miyasaka, "Organic-Inorganic Halide Perovskite Photovoltaics," *Org. Halide Perovskite Photovoltaics*, pp. 79–105, 2016, doi: 10.1007/978-3-319-35114-8_4.

[49] Y. Y. Kim *et al.*, "Fast two-step deposition of perovskite via mediator extraction treatment for large-area, high-performance perovskite solar cells," *J. Mater. Chem. A*, vol. 6, no. 26, pp. 12447–12454, 2018, doi: 10.1039/c8ta02868k.

[50] C. Liu, Y. Cheng, and Z. Ge, "Understanding of perovskite crystal growth and film formation in scalable deposition processes," *R. Soc. Chem.*, pp. 8–12, 2020, doi: 10.1039/c9cs00711c.

[51] H. Sun, P. Dai, X. Li, J. Ning, S. Wang, and Y. Qi, "Strategies and methods for fabricating high quality metal halide perovskite thin films for solar cells," *J. Energy Chem.*, vol. 60, pp. 300–333, 2021, doi: 10.1016/j.jechem.2021.01.001.

[52] Q. Wali, F. J. Iftikhar, M. E. Khan, A. Ullah, Y. Iqbal, and R. Jose, "Advances in stability of perovskite solar cells," *Org. Electron.*, vol. 78, no. December 2019, p. 105590, 2020, doi: 10.1016/j.orgel.2019.105590.

[53] M. cheol Kim, S. Y. Ham, D. Cheng, T. A. Wynn, H. S. Jung, and Y. S. Meng, "Advanced Characterization Techniques for Overcoming Challenges of Perovskite Solar Cell Materials," *Adv. Energy Mater.*, vol. 11, no. 15, pp. 1–26, 2021, doi: 10.1002/aenm.202001753.

[54] G. S. Patience, "Experimental methods and instrumentation for chemical engineers." Elsevier, Amsterdam; Boston, 2013, [Online]. Available: http://www.sciencedirect.com/science/book/9780444538048.

[55] J. I. Goldstein, D. E. Newbury, J. R. Michael, N. W. M. Ritchie, J. H. J. Scott,

and D. C. Joy, *Microscopy and X-Ray Microanalysis*. 2018.

[56] B. D. Cullity, *Elements of X-ray diffraction*. Utgivningsort ok�nd: Scholar's Choice, 2015.

[57] Y. Cheng *et al.*, "18% High-Efficiency Air-Processed Perovskite Solar Cells Made in a Humid Atmosphere of 70% RH," *Sol. RRL*, vol. 1, no. 9, p. 1700097, 2017, doi: 10.1002/solr.201700097.

[58] G. E. Eperon, S. D. Stranks, C. Menelaou, M. B. Johnston, L. M. Herz, and H. J. Snaith, "Environmental Science Formamidinium lead trihalide : a broadly tunable perovskite for e ffi cient planar heterojunction solar," pp. 982–988, 2014, doi: 10.1039/c3ee43822h.

[59] Y. Sun, J. Peng, Y. Chen, Y. Yao, and Z. Liang, "Triple-cation mixed-halide perovskites: Towards efficient, annealing-free and air-stable solar cells enabled by Pb(SCN) 2 additive," *Sci. Rep.*, vol. 7, no. January, pp. 1–7, 2017, doi: 10.1038/srep46193.

[60] M. Saliba *et al.*, "How to Make over 20% Efficient Perovskite Solar Cells in Regular (n-i-p) and Inverted (p-i-n) Architectures," *Chem. Mater.*, vol. 30, no. 13, pp. 4193–4201, 2018, doi: 10.1021/acs.chemmater.8b00136.

[61] M. Vásquez-montoya, J. F. Montoya, and D. Ramirez, "Understanding the precursor chemistry for one-step deposition of mixed cation perovskite solar cells by methylamine route," *J. Energy Chem.*, 2020, doi: 10.1016/j.jechem.2020.08.059.

[62] C. A. Otálora, G. Gordillo, L. Herrera, and J. Estrada, "Effect of the solution chemistry on the film growth of hybrid MAPbI3 perovskites," *J. Mater. Sci.*, no. 2, 2021, doi: 10.1007/s10854-021-05397-5.

[63] A. D. Taylor *et al.*, "A general approach to high-efficiency perovskite solar cells by any antisolvent," *Nat. Commun.*, vol. 12, no. 1, pp. 1–11, 2021, doi: 10.1038/s41467-021-22049-8.

[64] M. Samadpour *et al.*, "Modified Antisolvent Method for Improving the Performance and Stability of Triple-Cation Perovskite Solar Cells," *ACS Omega*, vol. 6, no. 1, pp. 172–179, 2021, doi: 10.1021/acsomega.0c04058.

[65] L. Tao *et al.*, "Stability of mixed-halide wide bandgap perovskite solar cells: Strategies and progress," *J. Energy Chem.*, vol. 61, pp. 395–415, 2021, doi: 10.1016/j.jechem.2021.03.038.

[66] Z. Yang *et al.*, "Stabilized Wide Bandgap Perovskite Solar Cells by Tin Substitution," 2016, doi: 10.1021/acs.nanolett.6b03857.

[67] N. Arora *et al.*, "Perovskite solar cells with CuSCN hole extraction layers yield stabilized efficiencies greater than 20%," vol. 771, no. November, pp. 768–771, 2017.

[68] T. Duong *et al.*, "Rubidium Multication Perovskite with Optimized Bandgap for Perovskite-Silicon Tandem with over 26 % Efficiency," vol. 1700228, pp. 1–11, 2017, doi: 10.1002/aenm.201700228.

[69] J. A. Christians *et al.*, "Tailored interfaces of unencapsulated perovskite solar cells for > 1 , 000 hour operational stability," *Nat. Energy*, vol. 3, no. January, pp. 68–74, 2018, doi: 10.1038/s41560-017-0067-y.

[70] S. H. Turren-Cruz, A. Hagfeldt, and M. Saliba, "Methylammonium-free, high-performance, and stable perovskite solar cells on a planar architecture," *Science (80-.).*, vol. 362, no. 6413, pp. 449–453, 2018, doi: 10.1126/science.aat3583.

[71] E. H. Jung *et al.*, "Efficient, stable and scalable perovskite solar cells using poly(3-hexylthiophene)," *Nature*, vol. 567, no. 7749, pp. 511–515, 2019, doi: 10.1038/s41586-019-1036-3.

[72] M. Kim *et al.*, "Methylammonium Chloride Induces Intermediate Phase Stabilization for Efficient Perovskite Solar Cells," *Joule*, vol. 3, no. 9, pp. 2179–2192, 2019, doi: 10.1016/j.joule.2019.06.014.

[73] H. Zhu *et al.*, "Tailored Amphiphilic Molecular Mitigators for Stable Perovskite Solar Cells with 23 . 5 % Efficiency," vol. 1907757, pp. 1–8, 2020, doi: 10.1002/adma.201907757.

[74] M. Jeong *et al.*, "Stable perovskite solar cells with efficiency exceeding 24.8% and 0.3-V voltage loss," vol. 1620, no. September, pp. 1615–1620, 2020.

[75] X. Wang *et al.*, "Engineering fluorinated-cation containing inverted perovskite solar cells with an efficiency of >21% and improved stability towards humidity," *Nat. Commun.*, vol. 12, no. 1, 2021, doi: 10.1038/s41467-020-20272-3.

[76] J. Zhang and H. Yu, "Multifunctional dopamine-assisted preparation of efficient and stable perovskite solar cells," *J. Energy Chem.*, vol. 54, pp. 291–300, 2021, doi: 10.1016/j.jechem.2020.05.061.

[77] A. Kojima, K. Teshima, Y. Shirai, and T. Miyasaka, "Organometal halide perovskites as visible-light sensitizers for photovoltaic cells," *J. Am. Chem. Soc.*, vol. 131, no. 17, pp. 6050–6051, 2009, doi: 10.1021/ja809598r.

[78] H. S. Kim *et al.*, "Lead iodide perovskite sensitized all-solid-state submicron thin film mesoscopic solar cell with efficiency exceeding 9%," *Sci. Rep.*, vol. 2, pp. 1–7, 2012, doi: 10.1038/srep00591.

[79] J. Burschka *et al.*, "Sequential deposition as a route to high-performance perovskite-sensitized solar cells," *Nature*, vol. 499, no. 7458, pp. 316–319, 2013, doi: 10.1038/nature12340.

[80] W. S. Yang *et al.*, "Iodide management in formamidinium-lead-halide-based perovskite layers for efficient solar cells," *Science (80-.).*, vol. 356, no. 6345, pp. 1376–1379, 2017, doi: 10.1126/science.aan2301.

[81] N. J. Jeon *et al.*, "A fluorene-terminated hole-transporting material for highly efficient and stable perovskite solar cells," *Nat. Energy*, vol. 3, no. 8, pp. 682–689, 2018, doi: 10.1038/s41560-018-0200-6.

[82] W. Kraus and G. Nolze, "POWDER CELL - a program for the representation

and manipulation of crystal structures and calculation of the resulting X-ray powder patterns," *J. Appl. Crystallogr.*, vol. 29, no. 3, pp. 301–303, Jun. 1996, [Online]. Available: https://doi.org/10.1107/S0021889895014920.

[83]   E. C. Ashby and R. D. Schwartz, "A glove box system for the manipulation of air sensitive compounds," *J. Chem. Educ.*, vol. 51, no. 1, pp. 65–68, 1974, doi: 10.1021/ed051p65.

[84]   L. A. Szolga and C. A. Stan, "Plexiglass glove box for organic solar cells," *IOP Conf. Ser. Mater. Sci. Eng.*, vol. 1032, no. 1, 2021, doi: 10.1088/1757-899X/1032/1/012048.

[85]   K. Kubota, R. Takahashi, and H. Ito, "Mechanochemistry allows carrying out sensitive organometallic reactions in air: Glove-box-and-Schlenk-line-free synthesis of oxidative addition complexes from aryl halides and palladium(0)," *Chem. Sci.*, vol. 10, no. 22, pp. 5837–5842, 2019, doi: 10.1039/c9sc01711a.

[86]   J. Wu, J. J. Dong, S. X. Chen, H. Y. Hao, J. Xing, and H. Liu, "Fabrication of Efficient Organic-Inorganic Perovskite Solar Cells in Ambient Air," *Nanoscale Res. Lett.*, vol. 13, 2018, doi: 10.1186/s11671-018-2714-z.

[87]   P. R. N. Childs, "Mechanical design engineering handbook." 2019, [Online]. Available: http://search.ebscohost.com/login.aspx?direct=true&scope=site&db=nlebk&db=nlabk&AN=1724744.

[88]   NIH, "Methylammonium Iodide," *PubChem Compound Database*, 2021. https://pubchem.ncbi.nlm.nih.gov/compound/519034 (accessed Nov. 12, 2021).

[89]   NIH, "Lead (II) iodide," *PubChem Compound Database*, 2021. https://pubchem.ncbi.nlm.nih.gov/compound/24931 (accessed Dec. 11, 2021).

[90]   SimScale, "What is von Mises Stress?," *SimScale Documentation*, 2021.

https://www.simscale.com/docs/simwiki/fea-finite-element-analysis/what-is-von-mises-stress/ (accessed Nov. 12, 2021).

[91] MatWeb, "MatWeb Material Property Data," 2021. http://www.matweb.com/search/DataSheet.aspx?MatGUID=632572aeef2a42 24b5ac8fbd4f1b6f77&ckck=1.

[92] D. Dabholkar, D. Shenvi, N. Anekar, and O. Joshi, "Design of Wet Leak Test Machine for Radiators: A Study," *Int. J. Curr. Eng. Technol.*, vol. 4, no. 4, pp. 343–346, 2016, doi: 10.14741/ijcet/22774106/spl.4.2016.68.

[93] A. Kumar, *Reservoir engineering handbook*. New Delhi: SBS Publ. & Distributors, 2012.

[94] D. B. Mitzi, *Solution Processing of Inorganic Materials*, 1st ed. Hoboken, N.J.: Wiley-Interscience, 2009.

[95] W. D. Callister.Jr, "Materials Science and Engineering An Intoduction," *J. Mater. Sci.*, vol. 7, no. 14, pp. 3940–3944, 2010.

[96] P. Boonmongkolras, D. Kim, and E. M. Alhabshi, "Understanding effects of precursor solution aging in triple cation lead perovskite," *RSC Adv.*, vol. 8, pp. 21551–21557, 2018, doi: 10.1039/C8RA03471K.

[97] M. S. Mehde, A. M. Al-Gebori, and A. K. Hantoosh, "The effect of the spinning speed variation on the perovskite solar cell efficiency," *IOP Conf. Ser. Mater. Sci. Eng.*, vol. 757, no. 1, 2020, doi: 10.1088/1757-899X/757/1/012071.

[98] J. Li, Q. Wang, and A. Abate, *Perovskite Solar Cells*, vol. 93, no. 9. Elsevier Inc., 2015.

[99] Y. Lv, Y. Jin, W. Cai, Z. Zhang, X. Zhou, and H. Chen, "Air-processed carbon-based perovskite solar cells with enhanced efficiency and stability: Effect of temperature control and using CuSCN," *J. Alloys Compd.*, vol. 821, p. 153272, 2020, doi: 10.1016/j.jallcom.2019.153272.

[100] M. Saliba *et al.*, "Cesium- containing triple cation perovskite solar cells: improved stabilty, reproducibility and high efficiency," *Energy Environ. Sci.*, vol. 9, no. 6, pp. 1989–1997, 2016, doi: 10.1039/c5ee03874j.

[101] L. Chen, C. Chen, J. Chen, and C. Wu, "ScienceDirect Annealing effects on high-performance CH 3 NH 3 PbI 3 perovskite solar cells prepared by solution-process," *Sol. ENERGY*, vol. 122, pp. 1047–1051, 2015, doi: 10.1016/j.solener.2015.10.019.

[102] D. V Amasev, S. R. Saitov, V. G. Mikhalevich, R. Tameev, and A. G. Kazanskii, "Effect of the heat treatment of CH 3 NH 3 PbI 3 perovskite on its electrical and photoelectric properties," *Mendeleev Commun.*, vol. 31, no. 4, pp. 469–470, 2021, doi: 10.1016/j.mencom.2021.07.010.

[103] T. Oku, "Crystal Structures and Related Perovskite Compounds Used for Solar Cells," in *Solar Cells New Approaches and Reviews*, One., L. A. Kosyachenko, Ed. InTech, 2015.

[104] A. Kogo, Y. Sanehira, Y. Numata, M. Ikegami, and T. Miyasaka, "Amorphous Metal Oxide Blocking Layers for Highly Efficient Low Temperature Brookite TiO 2 - based Perovskite Solar Cells," *ACS Appl. Mater. Interfaces*, 2018, doi: 10.1021/acsami.7b16662.

[105] C. Zhang *et al.*, "Effects of A site doping on the crystallization of perovskite films," *J. Mater. Chem. A*, vol. 9, no. 3, pp. 1372–1394, 2021, doi: 10.1039/d0ta08656h.

[106] M. Han, Z. Liu, X. Liu, J. Yoon, and E.-C. Lee, "Cesium Doping for Performance Improvement of Lead(II)-acetate-Bases Perovskite Solar Cells," *Materials (Basel).*, vol. 14, no. 363, 2021, doi: https://doi.org/10.3390/ma14020363.

[107] F. Ünlü, E. Jung, S. Öz, H. Choi, T. Fischer, and S. Mathur, "Chemical Processing of Mixed-Cation Hybrid Perovskites : Stabilizing Effects of

Configurational Entropy," in *Perovskite Solar Cells: Materials, Processes, and Devices*, M. Grätzel, S. Ahmad, and S. Kazim, Eds. 2021, pp. 1–31.

[108] J. Dutta, M. C. Ajith, S. Dutta, and U. R. Kadhane, "An inherent instability study using ab initio computational methods and experimental validation of Pb (SCN) 2 based perovskites for solar cell applications," *Sci. Rep.*, no. 0123456789, pp. 1–12, 2020, doi: 10.1038/s41598-020-72210-4.

[109] A. Halder *et al.*, "Pseudo -halide (SCN -) doped MAPbI 3 Perovskites : A Few Surprises," *J. Phys. Chem. Lett.*, 2015, doi: 10.1021/acs.jpclett.5b01327.